REVIEWS in MINERALOGY
Volume 37 1998

ULTRAHIGH-PRESSURE MINERALOGY

Physics and Chemistry of the Earth's Deep Interior

Russell J. Hemley, ***Editor***
Geophysical Laboratory
Carnegie Institution of Washington
Washington, DC

This volume was supported in part by

The Center for High Pressure Research

A National Science Foundation
Science and Technology Center

Paul H. Ribbe, ***Series Editor***
Department of Geological Sciences
Virginia Tech, Blacksburg, Virginia

MINERALOGICAL SOCIETY of AMERICA
Washington, DC

Chapter 6

LOWER MANTLE MINERALOGY AND THE GEOPHYSICAL PERSPECTIVE

Craig R. Bina

Department of Geological Sciences
Northwestern University
Evanston, Illinois 60208

INTRODUCTION

A variety of observations (Jeanloz 1995, Helffrich and Wood 1996, Irifune and Isshiki 1998, Agee this volume) suggest that the upper mantle may be largely peridotitic in bulk composition, perhaps approaching the composition of the model pyrolite (Ringwood 1989). What can be said about the composition and mineralogy of the lower mantle? Certainly we expect the mineralogy of the lower mantle to differ from that of shallower regions, if only due to high-pressure phase transformations, but why might the bulk composition of the lower mantle differ from that of the overlying material? Early partial melting of the mantle (Herzberg and O'Hara 1985) may have resulted in large-scale differentiation between upper and lower mantle, although elemental partitioning data appear not to support such a model (Kato et al. 1988). Diffusive (Garlick 1969, Bina and Kumazawa 1993) or convective (Weinstein 1992) processes acting across regions of phase transition may have generated chemical separation between upper and lower mantle, but such processes would occur over inordinately long time scales in the absence of fluid phases (Mao 1988). Perhaps more fundamentally, if chondritic meteorites (Anders and Grevesse 1989) are taken as representative of the cosmochemistry of the solar nebula from which the planet condensed, then a bulk earth whose whole mantle is of pyrolite composition (Ringwood 1989) is deficient in silicon. Unless the excess silicon was taken up in the core or volatilized during planetary accretion (Ringwood 1975), or unless the chondritic model is not an appropriate model for the bulk earth (McDonough and Sun 1995), then the lower mantle should be enriched in silica relative to a pyrolitic upper mantle. Early models of solar cosmochemistry indicated an iron deficit, suggesting that the lower mantle might be enriched in iron relative to the upper mantle (Anderson 1989a), but subsequent calibration of photospheric spectra (Holweger et al. 1990, Biémont et al. 1991) brought solar abundances into agreement with those of chondrites, thus removing the cosmochemical argument for iron enrichment.

Aside from a few diamond inclusions that appear to represent low-pressure, back-transformation products of lower mantle mineral assemblages (Kesson and Fitz Gerald 1991, Harte and Harris 1994, Harte et al. 1994), the lower mantle is not amenable to direct sampling. Thus, the mineralogy and composition of this region must be inferred via geophysical remote sensing, from (for example) observations of seismic waves and electric fields at the surface. The processing of raw geophysical data lies beyond the scope of this review, but an outline of how geophysical models are constructed (and exposure to their associated terminology) can give valuable insight into potential uncertainties. Furthermore, the models (e.g. three-dimensional seismic velocity structures) which result from inversion of these data can be used to construct models of lower mantle composition and mineralogy. Ideally, the resulting lower mantle mineralogical models could then be tested by using them to predict the primary geophysical observations, in the sort of forward modeling approach already applied in the transition zone (Helffrich and Bina 1994). Many uncertainties remain in our understanding of the geophysical properties of minerals under lower mantle conditions, so that conclusions tentatively drawn

0275-0279/98/0037-0006$05.00

herein may be subject to change in the wake of future measurements. However, while we may not yet be "in possession of the talismans which are to open to thee the mineral kingdoms and the centre of the earth itself" (Beckford 1786), the topics reviewed herein should provide a framework for addressing unanswered questions as more data become available.

RADIAL DENSITY AND VELOCITY PROFILES

Geophysical background

Deep earth structure is investigated seismologically by studying the propagation of waves excited by earthquakes (or nuclear explosions). These can be thought of as body waves (generally with periods of order 1 s), traveling along specific paths from source to receiver, or as superpositions of normal modes of free oscillation (generally with periods of order 100 s) of the entire planet. (They can also be thought of as surface waves, but these are seldom employed for lower mantle study.)

1-D velocities. The speeds with which body waves travel through the earth's interior are simply related to the density and elastic moduli of the material:

$$V_P^2 = (K_S + \tfrac{4}{3}\mu) / \rho \quad , \quad V_S^2 = \mu / \rho$$

where V_P is compressional wave (P-wave) velocity, V_S is shear wave (S-wave) velocity, ρ is density, μ is shear modulus, and K_S is adiabatic bulk modulus (used instead of the isothermal modulus K_T because the characteristic time of the passage of seismic waves is far shorter than that of thermal diffusion). P-waves, therefore, travel faster than S-waves in the same medium. When comparing the results of seismological studies to laboratory analyses of minerals, it is sometimes desirable to extract K_S in isolation from μ, because the former is often better constrained experimentally under deep mantle conditions than the latter. To this end, the "bulk sound velocity" V_ϕ is defined:

$$V_\phi^2 \equiv V_P^2 - \tfrac{4}{3} V_S^2 = K_S / \rho$$

Although no wave actually travels at this speed in the solid earth (Bina and Silver 1997), V_ϕ can be thought of as the speed of a sound wave in an equivalent liquid (because μ therein is always zero), and it can be measured in the laboratory from the slope of the (adiabatic) static compression curve. As mineralogical equations of state for $\mu(P,T)$ improve in quality, use of V_ϕ in earth models should decline in favor of the more physically realizable V_P and V_S.

An initial goal of body-wave studies is to determine functions $V_P(z)$ and $V_S(z)$ which describe the variation in seismic wavespeed with depth z. Because velocities generally increase with depth, seismic waves refract and bend toward the surface, with more the steeply descending waves traveling a greater distance from the source before reaching the receiver (Fig. 1a). Since the bending of the wave paths depends upon the velocity gradients, the dependence of the travel-times of particular seismic waves (e.g. direct S-waves, core-reflected P-waves, etc.) between source and receiver upon the distance between source and receiver (sometimes plotted as a "τ-p" rather than a time-distance relation) can be inverted for models of velocities as functions of depth (Lay and Wallace 1995). Like most inversions, the resulting velocity models are non-unique. Because they exhibit correlated uncertainties, one cannot draw simple errors bars on the velocity profiles; a change in velocity at one depth must be compensated by a different change at another depth. Furthermore, such inversions can exhibit strong dependence upon the starting model, so that a discontinuity in the initial profile, for example, may not vanish in the final profile even if its presence is not required by the data. Thus, uncertainties are more often illustrated by plotting several different velocity profiles that all fit the data

equally well, sometimes beginning from different starting models (Kennett et al. 1995, Montagner and Kennett 1996). In addition, the sensitivity of seismic waves to structure is frequency-dependent, so that shorter wavelengths are required to resolve finer features of the velocity profiles.

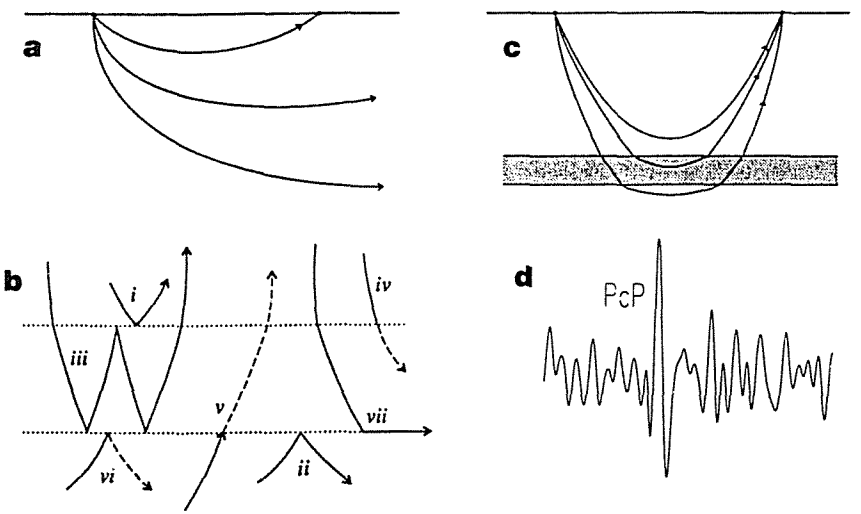

Figure 1. Seismic waves: Ray paths refract due to increase of velocity with depth (a). For sharp velocity gradients, deeper paths undergo greater refraction, resulting in a triplication (b). Boundary interactions phases (c) may reflect (i, ii), reverberate (iii), convert between P and S (iv, v), both reflect and convert (vi), or diffract (vii) at velocity discontinuities. Complete waveforms (d) contain more information than simply the travel times of identifiable waves (e.g. *PcP*).

Fine structure. Fine features such as rapid velocity changes can be resolved by study of additional properties of travel-time vs. distance behavior. At a given source-receiver distance, for example, a single direct P-wave will generally arrive at the receiver, and more steeply descending waves will arrive at more distant receivers (Fig. 1a). In a zone of rapid increase in velocity, however, more steeply descending waves will have their paths bent much more strongly than the more shallowly descending waves, so that two or three distinct pulses, separated in time, may arrive successively at the receiver from the gradient zone (Fig. 1b), in a phenomenon known as a "triplication." It was by observing such triplications that the major seismic velocity discontinuities in the mantle were first detected (Byerley 1926, Jeffreys 1936). A region of decrease in velocity, on the other hand, bends the wave paths oppositely, resulting in a "shadow zone" over which no pulse at all arrives from the gradient region (Lay and Wallace 1995).

Triplications and shadow zones arise by refraction of seismic waves as they pass through gradient zones. More detailed investigation of rapid changes in velocities with depth can be performed through study of "boundary interaction phases" (Clarke 1993): waves which are reflected, converted, or diffracted at gradient zones (Fig. 1c). Thus, waves may reflect off the topside (i) or underside (ii) of a boundary (Shearer 1991a), with underside reflections often appearing as precursors to waves which penetrated the boundary only later to reflect off of the underside of some shallower boundary (such as the earth's surface). Waves which reflect multiple times between boundaries (iii) are known as "reverberations," and because they spend so much time in the region between

boundaries they can serve as sensitive probes of the properties of such zones (Revenaugh and Jordan 1991a,b). When a *P*- or *S*-wave is incident upon a boundary, the individual wave may give rise to both transmitted *P*- and *S*-waves (with the restriction that *S*-waves cannot propagate in liquids) in a process known as "mode conversion," and such converted waves may arise on either downgoing (iv) or upgoing (v) paths. Such conversions may also generate reflected *P*- and *S*-waves, so that a boundary interaction phase may be both converted and reflected (vi). Finally, a wave incident upon a boundary may be "diffracted" so that it travels horizontally along the boundary itself (vii) before rising once again to a receiver (Wysession et al. 1992, Silver and Bina 1993, Garnero et al. 1993). Because such waves undergo fundamental changes in character at the boundary, their properties are sensitive to those of the boundary itself rather than only to average properties across a broader region, thus making them valuable probes of mantle fine structure.

For some time, seismologists focused upon the travel times of individual, identifiable waves, such as the distinct "*PcP*" reflection of a *P*-wave off of the core-mantle boundary (Fig. 1d). While study of such travel times reveals much about deep earth structure, much more information is contained in the complete waveforms, information such as the relative amplitudes of waves and the existence of interaction phases from previously unsuspected boundaries. Originally, synthetic waveforms were calculated only in a forward modeling approach, for relatively simple comparison with observed waveforms, but advances in numerical modeling now permit actual iterative "waveform inversion" for earth structure (Nolet 1990, Zielhuis and Nolet 1994, van der Lee and Nolet 1997).

All of these aspects of body-wave analysis can be brought to bear upon the study of rapid changes in seismic velocity or "discontinuities." For such features, important questions concern the depth, polarity (or sign), sharpness (or width), and magnitude (or brightness) of the associated velocity contrast. The depth at which a velocity contrast occurs can be determined from travel time vs. distance observations, but such estimates depend upon the models assumed for shallow velocity structure (Walck 1984). Better depth measurements can be obtained from boundary interaction phases by comparison to reference waves which undergo no boundary interaction, by comparison to reference waves with free surface interactions, or by measuring the differential times between arrivals of different boundary interaction phases. The polarity of a velocity contrast, whether it is a velocity increase or decrease, can be determined by looking for triplications or shadow zones in time-distance curves, or by comparing the upswing or downswing of boundary interaction phases to those of reference waves with either no boundary interaction or a free surface interaction. The sharpness of a velocity contrast, in terms of the depth extent over which it is largely complete, can be estimated from the frequency range over which observable boundary interaction phases are detectable: broader boundaries will not reflect well at shorter wavelengths. Sharpness can also be estimated from the spatial range over which a triplication is observable (Melbourne and Helmberger 1998), although this requires dense spatial coverage such as that afforded by an array. While relative amplitudes of boundary interaction phases can also provide sharpness information, their interpretation is generally model-dependent. Finally, the magnitude of a velocity contrast can be estimated from the change in slope of time-distance curves at triplications, but it is better determined from the amplitudes of boundary interaction phases relative to reference waves. Such amplitudes yield impedance contrasts, so that assumptions about densities are required to convert them to velocities, but the dependence of reflection coefficients upon density is relatively weak for waves with grazing paths (Lay and Wallace 1995). Both discontinuity sharpness and magnitude are generally more difficult to resolve than depth and polarity. Furthermore, the apparent magnitude, sharpness and depth measured by these methods will depend upon the frequencies of the seismic waves employed (Helffrich and Bina 1994).

Global averages. Radial velocity profiles can be constructed for specific regions (Grand and Helmberger 1984), or an attempt can be made to construct a globally-averaged profile (which may not correspond to real structure at any particular point on the earth). Global profiles generally suffer from a bias toward the structure beneath continents, because most receivers are located on land. Global profiles are also designed for differing purposes. While some (e.g. SP6 of Morelli and Dziewonski 1993) may represent attempts to model the actual globally-averaged structure of the earth, many (e.g. IASP91 of Kennett and Engdahl 1991, AK135 of Kennett et al. 1995) are designed primarily as "machines" for generating travel times for waves useful in locating earthquakes. Indeed, these latter often come with warnings attached, advertising their "relatively weak constraints on the details of the velocity distribution," noting that a "variety of styles of model give a similar level of fit to the data," and urging caution in interpreting them as any sort of "simple average of the earth" (Kennett and Engdahl 1991). The properties of discontinuities, in particular, are usually poorly resolved by such models. A picture of the global extent and properties of discontinuities can, however, be obtained by global stacking of a large number of seismograms in such a manner that signals representing laterally coherent structure are mutually reinforced while incoherent noise is damped through destructive interference (Shearer 1991b, Astiz et al. 1996).

Information on deep earth structure which is complementary to that obtained from body wave studies can also be gleaned by analysis of the earth's normal modes of oscillation as recorded on seismograms. Normal modes are equivalent to superpositions of many different body waves, and both the frequencies and amplitudes of these waves determine the resultant normal modes. As noted above in the context of body waves, the amplitudes (controlled by various reflection and transmission coefficients) depend upon impedance contrasts rather than simply velocity contrasts. Thus, measurements of the eigenfrequencies of such free oscillations allow construction of radial profiles of density (Masters 1979) as well as of *P*- and *S*-wave velocities (and also provide constraints upon anisotropy and anelasticity, as discussed later). Furthermore, modes of varying degrees (or spatial frequency) possess different profiles (or "kernels") of depth-sensitivity (Lay and Wallace 1995). Uncertainties in lower mantle ρ of the order of 0.10 g/cm^3 may arise due to choice of starting model and treatment of anisotropy and attenuation (Montagner and Kennett 1996). While such analyses yield good V_S resolution (1066A and 1066B of Gilbert and Dziewonski 1975), the low frequencies of most normal mode studies generally fail to resolve uncertainties in the fine structure of velocity and density profiles (Montagner and Kennett 1996).

Body wave data may be added to normal mode data in joint inversions for radial structure, thus providing improved V_P resolution as well (PREM of Dziewonski and Anderson 1981). However, differences in geographic biases, frequency bands, and sensitivity to anelasticity and anisotropy generally lead to systematic misfits with one data set or another. Recently, methods of reconciling the body wave and normal mode data sets have been explored, by first using body waves to constrain radial structure and discontinuities and then using the eigenperiods of normal modes to extract density, anelasticity, and anisotropy structure (Montagner and Kennett 1996).

Mineralogical interpretation

Given models of the radial variations of ρ, V_P, and V_S in the lower mantle, our goal is to calculate velocity and density profiles for a variety of candidate compositions, so as to ascertain the compositions whose predicted elastic properties best fit the seismological models. This may be done either by "adiabatic decompression" of lower mantle properties for comparison to aggregate mineral properties at zero pressure or by extrapolation of

mineral properties to lower mantle conditions. We adopt the latter approach here, so as to minimize the problems of parameter covariance associated with the former (Bukowinski and Wolf 1990), but recent work has shown how consistent results may be obtained from both approaches (Jackson 1998a). In accordance with a large body of experimental data, we shall begin by assuming that the lower mantle consists largely of assemblages of $(Mg,Fe)SiO_3$ silicate perovskite and (Mg,Fe)O magnesiowüstite, so that we can characterize a candidate composition by the two molar ratios:

$$X_{Mg} = Mg / (Mg + Fe) \quad , \quad X_{Pv} = Si / (Mg + Fe)$$

Equations of state. For each candidate composition, we wish to calculate densities and seismic wave velocities at a variety of lower mantle pressures and temperatures, so we require thermoelastic equations of state for the relevant minerals (Bina and Helffrich 1992, Duffy and Wang this volume, Liebermann this volume). Fundamentally, the required equations of state (EoS) must provide volume V as an explicit or implicit function of pressure P and temperature T. From such a $V(P,T)$ function, we can calculate both density ρ, from $\rho \equiv M / V$ where M is the molar mass, and bulk modulus K_T, from $K_T \equiv -V(\partial P / \partial V)_T$. A variety of EoS parameterizations may be employed, but it is common to write an EoS for the volume implicitly as $P(V,T)$, thus allowing the following differential expansion:

$$P(V,T) - P(V_0,T_0) = \int_{V_0}^{V} \left(\frac{\partial P}{\partial V}\right)_{T_0} d\hat{V} + \int_{T_0}^{T} \left(\frac{\partial P}{\partial T}\right)_{V} d\hat{T}$$

The first term on the right-hand side is often called the "cold" pressure, and its integrand can be written as $-K_T / \hat{V}$, evaluated at the initial temperature T_0, where K_T is the isothermal bulk modulus. The integral is usually evaluated via a finite strain formalism, such as the third-order Birch-Murnaghan equation:

$$P_{cold} = 3K_{T0} f (1 + 2f)^{5/2} (1 - \xi f)$$

$$f \equiv \tfrac{1}{2}\left[(V_0 / V)^{2/3} - 1\right] \quad , \quad \xi \equiv -\tfrac{3}{4}(K'_{T0} - 4)$$

where the reference isothermal bulk modulus K_{T0} and its pressure derivative K'_{T0} are evaluated at T_0 and V_0. Higher-order versions of the Birch-Murnaghan equation may also be employed. Similarly, a logarithmic strain formalism (Poirier and Tarantola 1998) could be used instead of this Eulerian finite strain formalism.

The second term on the right-hand side is generally called the "thermal" pressure, and its integrand can be written as αK_T or, equivalently, as $\gamma C_V / V$, evaluated at the final volume V, where α is the volume coefficient of thermal expansion, γ the Grüneisen parameter, and C_V the isochoric heat capacity. The integral can be evaluated using either notation, but the former generally leads to a class of EoS involving integrals of the Anderson-Grüneisen parameter,

$$\delta_T \equiv \frac{-1}{\alpha K_T}\left(\frac{\partial K_T}{\partial T}\right)_P = \frac{-K_T}{\alpha}\left(\frac{\partial \alpha}{\partial P}\right)_T$$

and some empirical form of polynomial expansion of $\alpha(T)$, such as:

$$\alpha(T) \approx \alpha_0 + \alpha_1 T + \alpha_2 T^{-2}$$

Arbitrary polynomial expansions can exhibit pathological behavior (e.g. negative temperature derivatives) at high temperatures and thus may not be optimal for extrapolating beyond the range of experimental data, although the example given above works well for $\alpha_0 > 0$, $\alpha_1 > 0$, and $\alpha_2 < 0$ because inflection points then lie in the domain of negative

temperatures.

The latter notation yields a different class of EoS, perhaps the simplest of which is the Mie-Grüneisen-Debye type:

$$P_{thermal} \approx \frac{\gamma_D}{V}\left[E_{th}(V,T) - E_{th}(V,T_0)\right]$$

$$E_{th}(V,T) \equiv 9nRT\left(\frac{\theta_D}{T}\right)^{-3} \cdot \int_0^{\theta_D / T} \frac{t^3}{e^t - 1}\, dt$$

$$\theta_D \equiv \theta_{D0}(V_0 / V)^{\gamma_D} \quad , \quad \gamma_D \equiv \gamma_{D0}(V_0 / V)^{-q}$$

where θ_{D0} and γ_{D0} are the reference Debye temperature and Grüneisen parameter, respectively, and q gives the volume dependence of the latter. This lattice dynamical approach to the EoS need not be restricted to the form of a Debye model, however. The thermal pressure can also be calculated from an explicit density of states, obtained from spectroscopic data, for example (Navrotsky 1994). Because such formalisms attempt to model the lattice dynamical behavior of crystals at high temperatures, they can prove useful for extrapolating beyond the range of experimental data for Debye-like (Anderson 1998) or more complex solids. Alternatively, a thermal pressure EoS can be obtained from simulation techniques such as molecular dynamics.

Derivation of such mineral equations of state involves fitting values to unknown coefficients by inverting from $V(P,T)$ measurements. Since these coefficients represent various derivatives of V, care must be take to ensure that coverage of the P-T space is adequate to constrain the values in question. Thus, while a given range of $V(P)$ data may be sufficient to constrain volume (and therefore density) over a certain range of pressure, the same data may not be sufficient to constrain bulk modulus (and therefore seismic velocity) or other P- and T-derivatives over that range. Such EoS uncertainties can often be fruitfully examined by determining the trade-offs among the various unknown coefficients to be fit to the data (Bell et al. 1987, Bina 1995).

Ideally, we would also like to have an additional equation of state for the shear modulus, $\mu(P,T)$, to allow us to calculate independent P- and S-wave velocities, V_P and V_S, at a variety of lower mantle pressures and temperatures. Such relations for shear moduli, however, currently remain relatively poorly constrained under lower mantle conditions. For this reason, the bulk sound velocity V_ϕ is often employed instead of the P- and S-wave velocities, because V_ϕ is independent of the shear modulus, as noted above. (The adiabatic and isothermal bulk moduli, employed in seismic velocities and equations of state, respectively, are related by $K_S = K_T(1 + T\alpha\gamma)$). Because shear moduli in many cases appear to be significantly more sensitive to variations in temperature and chemistry than bulk moduli, however, important advances in our understanding of the lower mantle can be expected to accompany improved constraints upon shear EoS in the future.

P, T, and K profiles. Having obtained suitable equations of state, for $V(P,T)$, $K_T(P,T)$, and possibly $\mu(P,T)$, we also require a profile of pressure $P(z)$ as a function of depth, which we can calculate by radial integration of the equation of hydrostatic equilibrium, $dP / dr = -\rho(r)g(r)$, where $\rho(r)$ is obtained from a seismological reference model such as AK135 (Kennett et al. 1995). Using the same $\rho(r)$ profile, $g(r)$ is calculated from Newton's law of gravitation, $g(r) = GM(r) / r^2$, where G is the gravitational constant and $M(r)$ the mass of that portion of the earth contained within a sphere of radius r.

Next, we require a profile of temperature $T(z)$ as a function of depth. It is common to begin by assuming such temperature profiles to be approximately adiabatic:

$$(\partial T / \partial P)_S = \alpha V T / C_P = \gamma T / K_S$$

Thus, given a starting temperature at the top of the lower mantle, we need merely perform a depth integration of:

$$dT / dz = g\alpha T / C_P = g\gamma T / V_\phi^2$$

where any slightly superadiabatic gradient can be accommodated simply by introducing a superadiabaticity factor:

$$\Delta T = \Delta P (\partial T / \partial P)_S (1 + f_{sup})$$

The olivine phase diagram indicates that, for the breakdown of γ silicate spinel (ringwoodite) to coincide with the 660-km seismic discontinuity, the temperature at 655 km should be approximately 1900 K (Ito and Katsura 1989). We can allow for uncertainty in this estimate by examining three different cases, where the starting temperature T_{LM} at 660 km is either 1800, 2000, or 2200 K.

Finally, because both (Mg, Fe)SiO_3 silicate perovskite (pv) and (Mg,Fe)O magnesiowüstite (mw) are solid solutions, we must constrain the elemental partitioning (Fei this volume) of Mg and Fe between these two coexisting phases. While the relevant molar partitioning coefficient,

$$K_{Mg-Fe}^{pv-mw} \equiv \frac{X_{Mg}^{mw} / X_{Fe}^{mw}}{X_{Mg}^{pv} / X_{Fe}^{pv}} = \frac{(1 - X_{Fe}^{mw}) X_{Fe}^{pv}}{(1 - X_{Fe}^{pv}) X_{Fe}^{mw}}$$

is commonly assumed to remain constant, we allow $K_{Mg-Fe}^{pv-mw}(P, T, X_{Mg})$ to vary by performing a trilinear fit to recent experimental partitioning data (Mao et al. 1997) that exhibit a dependence on P, T, and X_{Mg} (Fig. 2).

A worked example. Our fitting procedure is now straightforward. First, we assume a value of T_{LM}. Then we choose a candidate composition, characterized by values of X_{Mg} and X_{Pv}, to test. At each depth z we determine P and T. We then calculate K_{Mg-Fe}^{pv-mw} and thereby obtain X_{Fe}^{mw} and X_{Fe}^{pv}. Using these mineral proportions, along with the (Debye-like) EoS functions for each of the component minerals, we compute ρ for the mineral assemblage and the aggregate V_ϕ (or, ideally, V_P and V_S). We compare the latter to $\rho(z)$ and $V_\phi(z)$ from the reference seismological model and calculate the root-mean-square (RMS) misfit. We repeat this procedure for a set of (X_{Mg}, X_{Pv}) compositions and perhaps for several different values of T_{LM}.

There are two simple ways of examining the resulting set of misfit values to determine best-fitting lower mantle compositions. First, we can ask which uniform composition yields the minimum misfit summed over the full depth range of the lower mantle. This method provides, for each value of T_{LM}, two sets of ellipses in X_{Mg}-X_{Pv} space within which compositions yield RMS misfits to the seismological models for $\rho(z)$ and $V_\phi(z)$, respectively, that fall below some threshold misfits (Fig. 3). The orientations of the major axes of the misfit ellipses reveal the relative sensitivities of the two parameters: misfit to ρ is primarily sensitive to changes in X_{Mg} but not X_{Pv}, while misfit to V_ϕ is sensitive to changes in either. This graphically illustrates the fact that attempts to fit mantle density alone cannot constrain the silica content of the lower mantle; it is the intersection of these two ellipses which provides tight bounds on allowable mantle compositions. Indeed, the $\rho(z)$ and $V_\phi(z)$ misfit ellipses can be combined in an RMS sense (with, for simplicity, equal weighting) to give a single ellipse within which all compositions yield a joint RMS misfit to the seismological model that falls below some chosen threshold (Fig. 4). The variation in best-fit composition with changes in T_{LM} shows that, in general, a hotter lower mantle requires a greater silica content in order to match globally

averaged seismological models. Changes in assumed mineral EoS functions will, of course, also affect the resulting best-fit compositions, as will changes in reference seismic models (Birch 1952, Jackson 1983, Knittle et al. 1986, Jeanloz and Knittle 1989, Bina and Silver 1990, Stixrude et al. 1992, Hemley et al. 1992, Zhao and Anderson 1994, Jackson and Rigden 1998, Bina and Silver 1997, Jackson 1998a).

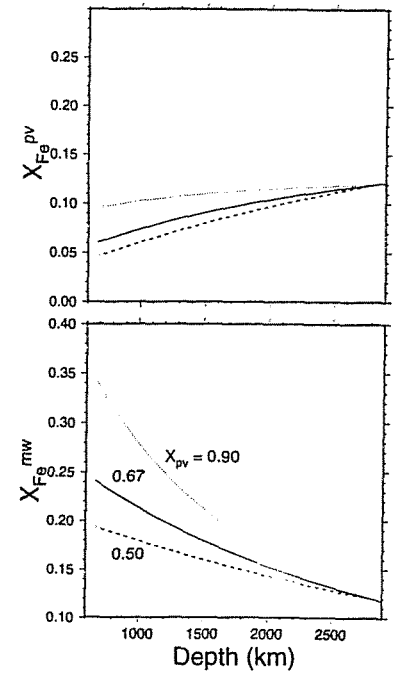

Figure 2 (right). Depth-dependent Fe-Mg partitioning between silicate perovskite (pv) and magnesiowüstite (mw). Mole fractions of Fe in coexisting pv and mw, for three bulk compositions of varying silica content, are derived from the data of Mao et al. (1997).

Figure 3 (below, left). Contours of RMS misfit between seismologically derived and mineralogically calculated profiles of $\rho(z)$ (dashed) and $V_\phi(z)$ (solid), constraining allowable lower mantle compositions in terms of iron and silica content. Contour interval is 0.5%. Triangle denotes pyrolite composition. T_{LM} is 2000 K. Perovskite thermal EoS from line 2 of Table 1 of Bina (1995) with cold EoS from Fabrichnaya (1995).

Figure 4 (below, right). Contours of joint RMS misfit between seismologically derived and mineralogically calculated profiles of $\rho(z)$ and $V_\phi(z)$, combined in an equally-weighted RMS sense, constraining allowable lower mantle compositions in terms of iron and silica content. Contour is 1.0%. Triangle denotes pyrolite composition. T_{LM} is 1800, 2000, and 2200 K (left to right). Perovskite thermal EoS from line 2 of Table 1 of Bina (1995) with cold EoS from Fabrichnaya (1995).

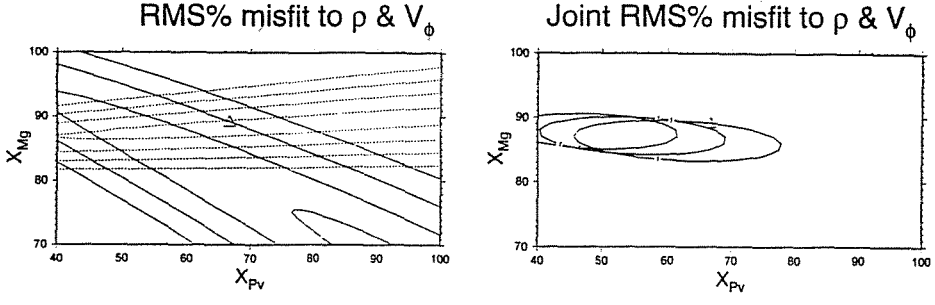

Second, we can ask which composition yields the minimum misfit at each individual depth, thus revealing how both the apparent best-fit lower mantle composition and the overall quality of the fit vary with depth (Fig. 5a). For T_{LM} of 2000 K, the effective value of K_{Mg-Fe}^{pv-mw} rises steadily from around 0.25 to near 1. While the best-fit value of X_{Mg} remains near that of an upper mantle pyrolite composition, the best-fit value of X_{Pv} begins near that of pyrolite and then falls gradually to lower values. The quality of the fit remains good throughout. The gradual drift in best-fit X_{Pv} value with increasing depth probably reflects, at least in part, the failure of our chosen EoS to faithfully describe the elastic behavior of lower mantle minerals as we extrapolate to great depths beyond the range of measured data. For a markedly different (non-Debye-like) EoS for silicate

perovskite (Fig. 5b), the best-fit value of X_{Mg} remains near that of an upper mantle pyrolite composition, with somewhat greater scatter. The best-fit value of X_{Pv}, on the other hand, begins significantly enriched in silica relative to pyrolite and then falls steeply to lower values. The quality of the fit gradually improves to about 1700 km depth and remains good thereafter. The steep decline in best-fit X_{Pv} value with increasing depth probably also reflects faults in the extrapolatory behavior of our EoS, but the problems with this EoS appear to be more severe than in the previous case. Such defects are also suggested by the surprisingly poor quality of fit for the initially high values of X_{Pv}, even at relatively shallow depths.

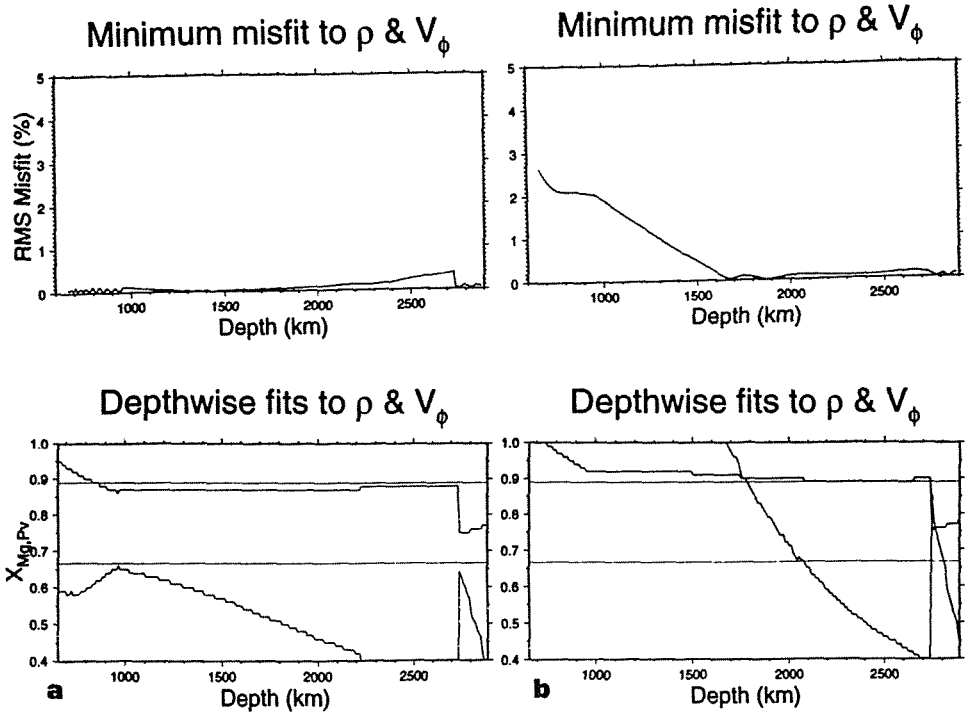

Figure 5. Joint RMS misfit between seismologically derived and mineralogically calculated $\rho$and V_ϕ, combined in an equally-weighted RMS sense, and best-fit compositions, in terms of iron and silica content, all as functions of depth in the lower mantle, for T_{LM} of 2000 K. Fitting performed for Debye-like (a) and non-Debye-like (b) perovskite equations of state (thermal EoS from line 2 and line 1, respectively, of Table 1 of Bina 1995, with cold EoS from Fabrichnaya 1995). Dotted lines denote pyrolite composition.

It is clear from these analyses that the best-fit compositions deviate markedly at the very top and bottom of the lower mantle. This is not surprising, because thermal, mineralogical, and chemical phenomena in these regions give rise to significant uncertainties and lateral variations in the velocity gradients and discontinuities of seismological models. Complex structure in the topmost lower mantle may arise from several sources, including temperature-induced topography on the phase boundary marking the top of the lower mantle (Bina and Helffrich 1994), possible stability of silicate ilmenite in the topmost lower mantle in cold regions of subduction (Reynard et al. 1996, Reynard and Rubie 1996, Irifune et al. 1996), and extension of the garnet stability field into the topmost lower mantle due to Al-Fe^{3+} coupling between ringwoodite, silicate perovskite, and garnet phases (Wood and Rubie 1996). The bottommost lower mantle (Jeanloz and Williams this volume) is believed to be a region of chemical changes, arising from interactions with the core or accumulation of subducted material, and may also feature additional high-pressure phase changes. Hence, these two regions are generally omitted from the calculations when using the first method detailed above to determine which uniform composition yields the minimum misfit summed over the lower mantle.

Further work. Many secondary effects have been neglected in the above analyses. For example, consideration of oxygen fugacity and defect chemistry may introduce Fe^{3+} substitution for Fe^{2+} or non-stoichiometry in magnesiowüstite, and charge-coupled substitutions may allow uptake of Al and Fe^{3+} and possibly Na into silicate perovskite. The effects of such solid solution phenomena on elastic properties remain poorly constrained at present. The accessory cubic $CaSiO_3$ perovskite phase has also been ignored here, but recent studies (Wang et al. 1996) suggest that its effects upon the aggregate elastic properties of lower mantle assemblages should be minimal. Given suitable measurements of elastic properties for such phases, these effects could be accounted for in future analyses by incorporation of additional molar ratios, such as X_{Ca} or X_{Al}, into the compositional parameterization.

Other potential phase changes have also been neglected in these analyses. Both $(Mg,Fe)SiO_3$ and $CaSiO_3$ perovskites may undergo structural distortions under deep mantle conditions, and high-pressure phase changes observed in FeO may also occur in lower mantle (Mg,Fe)O. Stabilization of higher pressure phases of SiO_2 or Al_2O_3 or pressure-induced changes in the maximum solubility of $FeSiO_3$ may induce disproportionation of perovskites into mixed oxides under certain conditions. Order-disorder phenomena may play a role in elemental partitioning. Additional experimental information on the relevant stability fields and equations of state will be required to fully treat such effects, but both the apparent absence of globally coherent seismic velocity discontinuities within the bulk of the lower mantle and the absence of evidence for major transformations in recent experiments under deep lower mantle conditions (Kesson et al. 1998) suggest that such effects may be more important in understanding local or lateral variations in temperature, composition, or seismic velocity than in explaining globally averaged models.

LATERAL SEISMIC VELOCITY HETEROGENEITY

Geophysical background

Proceeding from a model of how velocities and densities vary radially in a particular region or in a globally averaged earth, we now ask how these properties vary laterally in the earth as well. To our list of questions about discontinuities (depth, polarity, sharpness, magnitude), we now add lateral variability of all of these properties, including the question of over what spatial extent the velocity contrast is detectable at all. One obvious approach is to look for differences between radial profiles constructed for different regions. However, this is complicated by the dependence of the radial profiles upon their various starting models and by the fact that variations in mantle structure trade off against assumed shallow structure (Walck 1984). Given a large enough geographic distribution of boundary interaction points, however, such a method can be applied to the study of discontinuities, and constraints upon depth variations or "topography" of discontinuities can be further enhanced by evidence of focusing or defocusing in the amplitudes of boundary interaction phases (van der Lee et al. 1994).

Tomographic imaging. An increasingly popular method, however, is the direct inversion of travel times or other data for two- or three-dimensional structure, in a method known as "tomography." Seismic tomography employs the delay times or waveforms of identifiable seismic waves to map the spatial distribution of velocity

perturbations relative to a reference model (Su et al. 1994, Li and Romanowicz 1996, Grand et al. 1997, van der Hilst et al. 1997). When interpreted conservatively, the 3-D maps or "images" that result from tomographic modeling can powerfully illuminate both radial and lateral heterogeneity.

Tomography is subject to a variety of resolution limits (Spakman and Nolet 1988, Spakman et al. 1989) and other distortions (van der Hilst et al. 1993, Liu et al. 1998). In particular, the amplitudes of velocity perturbations may not be particularly well constrained, leading to possible underestimation of velocity anomalies, due to a variety of effects. The coarse parameterization of small-scale structure, for example, means that an anomaly smaller than the "cell size" of the model volume elements will be distributed as an average velocity perturbation across the entire cell: a 10-km-wide velocity gradient cannot be resolved in a model whose cells have 100-km edge lengths. Thus, models are sometimes constructed so that anticipated discontinuities (e.g. at 660 km) coincide with the boundaries, rather than penetrate the bodies, of model volume elements (or "voxels").

Another issue concerns the density and orientation of rays sampling any given cell (Fig. 6a). Cells with higher "hit counts" — i.e. those which are sampled by a greater number of rays (which are actually more like tubes in that they sample finite cross-sectional areas or "Fresnel zones" which depend upon frequency) — will have a greater influence upon the inversion, so that velocity perturbations contained in such cells may be better resolved. However, if a given ray samples a velocity anomaly (Fig. 6a), producing a delayed arrival at a receiver, the anomaly could be located anywhere along that ray path, resulting in "streaking" or "smearing" along rays which sample structure in a preferred direction. Most inversions seek to minimize such streaking by incorporating rays which intersect at various angles, so that the placement of the anomaly will be constrained by whether or not the various intersecting rays are delayed as well. Recent developments also allow the use of irregularly sized cells whose geometry can evolve during the inversion (Sambridge and Gudmundsson 1998).

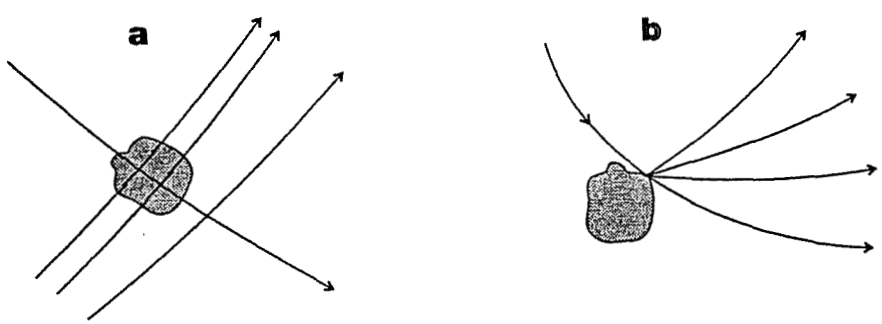

Figure 6. Seismic imaging: Tomographic resolution is limited by (a) the density of rays which sample a velocity anomaly and the fraction of those which intersect each other. Seismic waves may scatter energy (b) off of heterogeneities.

Subtler issues involve the choice of reference model (van der Hilst et al. 1989, Fukao et al. 1992). Ray paths computed from the reference model are used to locate velocity anomalies, but these paths should be recomputed for the perturbed model (VanDecar et al. 1995, Wolfe et al. 1997). Neglect of such corrections may skew results from a "checkerboard test," commonly used to estimate spatial resolution, in which a preselected pattern of velocity perturbations is numerically sampled by the same ray paths

associated with the real data, and the resulting synthetic data are inverted to discover how well the original pattern is recovered. The uniform distribution of rays arising from a smooth reference model may recover the input pattern well, but use of the perturbed model may reveal areas of less uniform resolution. Furthermore, tomographic images constructed through linear perturbation to homogeneous (essentially 1-D) reference models may yield inhomogeneities larger than are strictly suitable for linear perturbation theory. Recent developments allow inversions to be performed relative to heterogeneous (i.e. 3-D) reference models (Geller and Hara 1993) and without restriction to weak perturbations (Cummins et al. 1997).

Thus far we have presupposed complete knowledge of the locations of sources and receivers. The uncertainties attending earthquake locations, however, require joint inversion for source mislocation along with velocity structure, resulting in reduced amplitudes for perturbations. Furthermore, the inherent non-uniqueness of inversions means that a variety of velocity structures will fit the data equally well, so one must adopt some sort of measure to penalize certain types of structures in favor of others. To account for the variety of resolution issues discussed above, some sort of damped solution is generally sought. While "norm" damping favors models which differ minimally from the reference model, biasing models toward small perturbation amplitudes, "gradient" damping favors smooth models with minimal variations between adjacent cells. Combinations of these methods can be employed (van der Hilst et al. 1997), with some subjective choice of relative weighting between the two.

Despite these various resolution issues, most of which can be treated by suitable weighting and damping (or "regularization"), the results of tomographic inversions show a remarkable consensus in structural features, such as slab penetration into the lower mantle. Other images of lower mantle heterogeneity suggest sheet-like downwellings (Grand et al. 1997, van der Hilst et al. 1997) and regional deep mantle discontinuities with significant topography (Kawakatsu and Niu 1994, le Stunff et al. 1995, Niu and Kawakatsu 1997). Indeed, efforts at mineralogical interpretation of 3-D structure may most profitably focus upon such robust observations, demonstrated by agreement between independent inversions involving different data sets, damping choices, or other assumptions. The largest remaining uncertainties in tomographic imaging probably concern the amplitudes of velocity perturbations and the apparent scale lengths of heterogeneity. Additional errors may arise, however, from approximations in the theory, such as the common assumption of isotropic media. Given that neglect of velocity anisotropy (discussed below) can have significant effects upon inversion for 1-D reference models (Montagner and Kennett 1996), it is reasonable to expect similar effects in inversion for 3-D models.

Other observations. While a classical tomographic inversion is based solely upon travel times (Zhou and Clayton 1990, Grand 1994), additional constraints upon 3-D velocity structure can be obtained by expanding the variety of constraints to include both local and teleseismic data (Zhao et al. 1994), a priori constraints derived from boundary interaction phases (Zhao and Hasegawa 1993), actual waveforms, or free oscillation data. Indeed, by incorporating such a variety of data, one can extract constraints on the 3-D structure not only of velocities but also of density, attenuation, and anisotropy. However, expanding the number of free parameters can lead to instability in the inversion, especially if factors such as the differing frequency ranges or polarizations of various components of the data set are not properly taken into account.

It can be useful to check the regional structures illuminated by tomography by using another technique. For example, waveform modeling of triplicated seismic waves in the northwest Pacific (Tajima et al. 1998) yields smaller volumes for velocity anomalies than obtained from tomography in the same region. Another method, complementary to

tomography, employs scattering theory, using data collected across a seismographic array to locate a volume that consistently scatters energy (Fig. 6b) from several sources (Kaneshima and Helffrich 1998). Scattering observations yield information on the spectrum of spatial heterogeneities, and joint likelihood methods may then be employed to constrain the locations of individual scatterers. Such scattering studies can detect energy from smaller features than are presently resolvable by tomography, and comparisons between results from the two methods can further constrain the size of mantle velocity anomalies (Castle 1998).

Global seismological observations suggest that the lower mantle is more laterally homogeneous than the upper mantle (Gudmundsson et al. 1990) and that the characteristic spatial wavelengths of heterogeneity increase near the bottom of the lower mantle (Su et al. 1994). While evidence for strong (>2%) V_S heterogeneity at large (~200 km) scales in the lower mantle appears to be sparse (Nolet and Moser 1993), weaker (~2%) lower mantle V_P heterogeneity at small (<8 km) scales may be common (Hedlin et al. 1997), and strong heterogeneities may be present at different length scales.

Mineralogical interpretation

For any given seismic velocity anomaly, it is important to determine the polarity, magnitude, and sharpness of velocity contrasts at the boundary of the region, as well as (if possible) the spatial extent of the anomalous region. We can gain an idea of what sort of phenomena might give rise to such anomalies by investigating the partial derivatives of mineral elastic properties under lower mantle conditions.

P-, T-, and X-dependence. The temperature dependence of velocity, $(\partial V_\phi / \partial T)_{P,X}$, is about -2×10^{-4} km/s/K at 1000 km, falling to -1×10^{-4} km/s/K at 2000 km (varying slightly with composition). Thus, a ΔT of 100 K yields a ΔV_ϕ of -0.01 to -0.02 km/s, about the same as that arising from ΔP due to decreasing z by 10 km, because the pressure dependence of velocity, $(\partial V_\phi / \partial P)_{T,X}$, is ~0.03 km/s/GPa. Dynamical implications should also be considered when attempting to interpret velocities in terms of purely thermal anomalies. Given that $(\partial \rho / \partial T)_{P,X}$ is about -9×10^{-5} g/cm^3/K at 1000 km, rising to -7×10^{-5} g/cm^3/K at 2000 km (varying slightly with composition), a ΔT of 100 K would also yield a $\Delta \rho$ of -0.007 to -0.009 g/cm^3, so that inference of large thermal anomalies might also require the presence of significant density (i.e. buoyancy) anomalies which could prove dynamically unstable. Time scales should also be considered when interpreting velocity anomalies of thermal origin, especially if the putative thermal anomalies are believed to have arisen from the subduction process. For example, a slab thermal anomaly of ~1000 K would yield a lower mantle V_ϕ anomaly of a few ~0.1 km/s. If the velocity change were localized over ~10 km, the temperature anomaly would drop to nearly 1/3 of its initial value in about 10^6 years: (*time*) ≈ (*length*)^2 / (*diffusivity*). For slab material to reach a depth of 1000 km at a subduction rate of 10 cm/yr, however, would require 10^7 years. Thus, a ΔV_ϕ anomaly of a few ~0.1 km/s over 10 km, located below a depth of 1000 km, is unlikely to be due solely to a thermal anomaly associated with subducted material.

Time scales are not so relevant to anomalies of chemical origin, given the extremely long time scales of solid-state diffusion (Zindler and Hart 1986, Hart and Zindler 1989). The Mg-Fe composition dependence of velocity, $(\partial V_\phi / \partial X_{Mg})_{P,T}$, is about 1.1 km/s at 1000 km, rising to 1.4 km/s at 2000 km, so that a 0.01 increase in X_{Mg} yields ΔV_ϕ of ~0.01 km/s (varying slightly with Si content). Thus, small changes in local Mg/Fe ratio can produce velocity anomalies of the same general magnitude as those due to 100-K temperature perturbations. Similarly, the Si composition dependence of velocity, $(\partial V_\phi / \partial X_{Pv})_{P,T}$ is about 0.9 km/s at 1000 km, falling to 0.7 km/s at 2000 km (varying slightly with Mg content), but this latter systematicity may appear deceptively simple.

With increasing z, Si sensitivity for the Mg component falls while that for the Fe component rises, so that the bulk Si sensitivity (which falls for Mg_{90}) might actually rise with increasing z for a more Mg-poor composition. Nonetheless, to a first approximation, a 0.01 increase in X_{Pv} yields ΔV_ϕ of ≲0.01 km/s. So that, again, small changes in local Si content can produce velocity anomalies comparable to those arising from 100-K temperature anomalies. To the extent that lateral velocity variations may be due to compositional heterogeneity, such variations in major element chemistry need not necessarily correspond to the observed minor or trace element geochemical heterogeneity in the mantle (Hoffmann 1997). Nonetheless, either type of distributed chemical heterogeneity may persist in relatively unmixed form over geological time scales even in an actively convecting mantle (Davies 1990, Kellogg 1992, 1993; Metcalfe et al. 1995).

The dependence of velocity upon change in phase, $(\partial V_\phi / \partial X^{phase})_{P,T}$, may also contribute to velocity anomalies in important ways. A local thermal anomaly, for example, may shift a volume of material into a different stability field via a phase transformation, and these two effects can conspire to double the effective velocity anomaly (Bina 1998a). For this reason, phase diagrams should be checked for proximity of local P,T conditions to a reaction boundary when evaluating the potential effects of thermal anomalies. An attempt to interpret such a velocity anomaly in terms of temperature alone would yield a ΔT which exceeded the actual value by 100%. Furthermore, chemical anomalies may have similarly complex effects. A local increase in Fe content, for example, if it exceeded the maximum solubility of $FeSiO_3$ in perovskite under the prevailing P,T conditions (Fei et al. 1996, Wang et al. 1997, Mao et al. 1997), might induce breakdown to oxides, with consequent dramatic changes in V_ϕ.

V_P / V_S relations. Ideally, we would interpret lateral heterogeneity in terms of actual V_P and V_S instead of our proxy V_ϕ. However, such interpretations remain difficult at present, because the various derivatives of the shear moduli, especially under lower mantle P,T conditions, remain poorly known. This is particularly unfortunate, because V_S and the V_P / V_S ratio, sometimes expressed in terms of Poisson's ratio σ:

$$\sigma \equiv \frac{3K_S - 2\mu}{2(3K_S + \mu)} = \frac{1}{2}\frac{(V_P / V_S)^2 - 2}{(V_P / V_S)^2 - 1}$$

appear to be more sensitive to temperature and compositional changes than either V_P or V_ϕ. Global seismological studies indicate that $d \ln V_S / d \ln V_P$, a measure of the relative lateral heterogeneity in V_S and V_P, rises from about 1.7 to 2.6 with increasing depth in the lower mantle (Robertson and Woodhouse 1996), increasing to more than 3 in the mantle's bottommost few hundred kilometers (Bolton and Masters 1996). If we assume that all such lateral heterogeneity is due to thermal anomalies, then from ratios of temperature derivatives at constant pressure and composition we obtain:

$$\left(\frac{\partial \ln V_S}{\partial \ln V_P}\right)_{P,X} = \frac{\frac{K_S}{\mu} + \frac{4}{3}}{\frac{K_S}{\mu}\left(\frac{1-\delta_S}{1-\zeta}\right) + \frac{4}{3}}$$

where

$$\delta_S \equiv \frac{-1}{\alpha K_S}\left(\frac{\partial K_S}{\partial T}\right)_P \quad , \quad \zeta \equiv \frac{-1}{\alpha \mu}\left(\frac{\partial \mu}{\partial T}\right)_P$$

For reasonable mineralogical values of these parameters at the top of the lower mantle (Anderson 1989b), this ratio should adopt values of 1 to 2. The seismic observations of larger values thus suggest that the temperature-dependence of μ becomes progressively

stronger than that of K_S with increasing depth. However, the similar magnitudes of the various partial derivatives noted above allow ambiguity to remain regarding the relative degrees of thermal or compositional origin for lower mantle velocity heterogeneity, resolution of which awaits better constraints upon δ_S and ζ for perovskite-magnesiowüstite aggregates under deep lower mantle conditions (Stacey 1998).

SEISMIC VELOCITY ANISOTROPY

Geophysical background

Seismic heterogeneity, comprising lateral variations in P- and S-wave velocities from place to place, must further be distinguished from seismic anisotropy, in which velocities of P- and S-waves in any given location may vary with direction of propagation. Indeed, velocity anomalies due to anisotropy can be larger in magnitude than those arising from variations in temperature or composition and can exhibit significant lateral variation (Anderson 1989b). As macroscopic consequences of the fact that many rock-forming minerals exhibit directional variations in both V_P and V_S, seismic constraints upon elastic anisotropy in earth's interior are obtained by observing such phenomena as S-wave splitting (Vinnik et al. 1984, Ando 1984, Fukao 1984, Silver and Chan 1988, 1991; Kaneshima and Silver 1995, Fischer and Wiens 1996, Fouch and Fischer 1996), diffracted waves (Vinnik et al. 1995), converted waves (Vinnik and Montagner 1996), and free oscillations (Montagner and Kennett 1996). In attempting to differentiate the seismological signature of anisotropy from that of heterogeneity, it is important to distinguish the manner in which the seismic anisotropy is observed. In particular, it is useful to distinguish between observation of propagation and polarization anisotropy (Silver 1996).

Propagation and polarization. Propagation anisotropy is perhaps the simplest manifestation of the fact that V_P and V_S vary with direction of propagation. By observing the travel times of seismic waves that have sampled the same region but have traveled through it in different directions along different paths, the fast and slow directions for each of V_P and V_S may be deduced. However, because these waves have traveled along different paths, each may also have sampled different material outside the region of overlap. Thus, such observations admit a significant trade-off between anisotropy and heterogeneity (lateral variation in isotropic structure).

Polarization anisotropy, on the other hand, is a manifestation not only of anisotropy but also of the fact that particle motions for S-waves may be plane polarized. Hence, even along a single path in an anisotropic medium, S-waves will travel with different velocities V_S depending upon their polarization directions, described by the orientations of their particle motions within a plane quasi-orthogonal to that path. One consequent effect is that an initially arbitrarily polarized S-wave passing through a homogeneous anisotropic medium will be split into waves traveling at different speeds with different polarizations (Fig. 7a), a phenomenon known as "shear-wave splitting." Thus, because polarization anisotropy can be characterized by utilizing a single path, such analyses exhibit no trade-off between anisotropy and heterogeneity for the splitting of S-waves (although they do experience some trade-off for surface waves in the upper mantle).

Symmetry frameworks. Observations of seismic anisotropy are interpreted within the framework of simplified symmetry models (Crampin 1984, Babuska and Cara 1991, Silver 1996), which usually assume hexagonal (i.e. cylindrical) symmetry of the elastic properties of aggregate mantle material. Whereas an isotropic medium possesses 2 independent elastic moduli, one with hexagonal symmetry has 5 (compared to 9 for orthorhombic, 13 for monoclinic, or 21 for triclinic). One such model is that of transverse isotropy (also called radial anisotropy), in which the bulk material is assumed to possess hexagonal symmetry about a vertical axis (Fig. 7a), such as might arise from a

simply layered fabric. For such a symmetry, horizontally traveling waves will consist of a horizontally polarized P-wave (PH) and two S-waves (horizontally polarized SH and vertically polarized SV) of differing velocities. Vertically traveling waves, on the other hand will comprise a vertically polarized P-wave (PV) and two S-waves, the latter of which are orthogonally polarized in the horizontal plane and possess identical velocities equal to that of the horizontally traveling SV-wave. If the anisotropy is due to planar layering of isotropic media, the horizontally polarized S- and (horizontally propagating) P-waves will have faster velocities than their vertically polarized counterparts, but this need not be true for for anisotropy arising from inherently anisotropic crystals. Such anisotropy can be characterized using a variety of parameterizations. One commonly used to represent earth models (Montagner and Kennett 1996) consists of specifying the two velocities V_{PH} and V_{SV} along with three anisotropic parameters: ξ, given by the ratio $(V_{SH} / V_{SV})^2$ and analogous to mineralogical c_{66} / c_{44}; ϕ, given by $(V_{PV} / V_{PH})^2$ and analogous to c_{33} / c_{11}; and η, which describes velocity variations in off-axis propagation directions and is analogous to $c_{31} / (c_{11} - 2c_{44})$; where ξ, ϕ, and η are all unity for an isotropic medium.

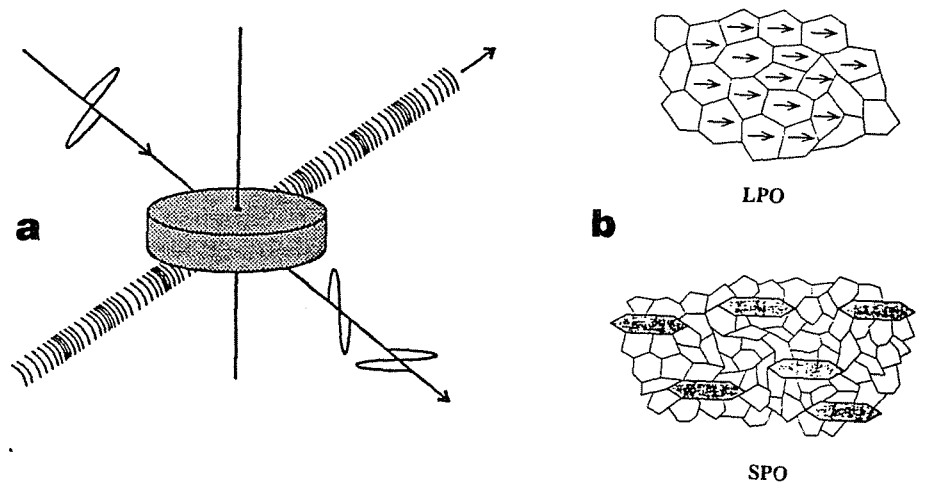

Figure 7. Elastic anisotropy: Cylindrically symmetric seismic anisotropy (a), showing a propagating P-wave and a split S-wave. Elastic anisotropy in mineral aggregates may arise (b) from lattice preferred orientation (LPO) of anisotropic crystals or from shape preferred orientation (SPO) of aligned inclusions with distinct elastic properties.

Another symmetry model, often employed in lithospheric studies, is that of azimuthal anisotropy. The most common form of this model is fundamentally a model of transverse isotropy rotated through 90°, in which the bulk material is assumed to possess hexagonal symmetry about a horizontal axis, such as might arise as oceanic lithosphere spreads away from a mid-ocean ridge forming a preferred orientation lineation (Christensen and Crosson 1968). In this case, horizontally traveling waves propagating along the symmetry axis will consist of a P-wave and two S-waves of equal velocities, but those propagating in other directions, whether horizontally or vertically, will comprise a P-wave and two S-waves of differing velocities. It is in this framework that observations of S-wave splitting from nearly vertically propagating shear waves are interpreted. For example, a particular S-wave, SKS, becomes plane polarized at the core-mantle boundary and travels nearly vertically upwards through the mantle. If it passes through anisotropic material, it becomes split into two orthogonally polarized S-waves traveling at different

speeds. From observations of such waves as they arrive at the surface, both the polarization direction (in the horizontal plane) of the fast S-wave and the delay time between the fast and slow arrivals can be determined, where the latter is a function of both the magnitude of velocity anisotropy and the physical extent of anisotropic material (Silver 1996).

While transverse isotropy is usually assumed in modeling the whole earth, shear-wave splitting provides evidence of azimuthal anisotropy in the upper mantle. Clearly, these simplified models cannot both be correct for the same region, although transverse isotropy can be viewed as a spatial average of azimuthal anisotropy if the symmetry axis for the latter is randomly distributed in the horizontal plane. Furthermore, individual mantle minerals usually do not possess a symmetry as simple as hexagonal (e.g. orthorhombic olivine with 9 moduli), although they may exhibit a simpler effective symmetry in aggregates. Surface waves have been used to image upper mantle anisotropy in a more complex framework involving both radial and azimuthal components, with results that suggest that S-wave azimuthal anisotropy becomes insignificant below 300 km (Montagner and Tanimoto 1991). Wave interaction with non-planar interfaces can further complicate the signature of anisotropy, as can non-uniformity of symmetry axis orientation. Indeed, when S-wave splitting occurs in regions of varying anisotropy, the orthogonal polarization planes can rotate about the propagation direction, complicating interpretation of the apparent fast polarization direction (Babuska and Cara 1991). Nonetheless, interpretation of seismic data within these simple uniformly hexagonal frameworks generally works well (e.g. effectively eliminating *SKS* energy from the transverse components of seismograms and reducing elliptical to linear particle motions) and provides a useful integral constraint on overall anisotropy. Complications can arise when the apparent splitting parameters vary with the direction of the incoming waves, which may signal deviation from a simple hexagonal model or violation of the assumption of a strictly vertical symmetry axis, or when they vary with the initial polarization of the incoming waves from a single direction, which may indicate the presence of multiple anisotropic layers (Silver and Savage 1994). Of course, vertically propagating S-waves yield poor resolution of the depth of any anisotropic material, so special geometries involving combinations of waves traveling along different paths must be used to determine the depths of anisotropic regions.

Lower mantle isotropy. The bulk of the lower mantle, however, appears to be largely elastically isotropic (Kaneshima and Silver 1995, Fischer and Wiens 1996, Fouch and Fischer 1996, Montagner and Kennett 1996). Any significant level of azimuthal anisotropy should be evident when integrated over the large path lengths of seismic waves in the lower mantle, yet none is observed (Meade et al. 1995). Measurable anisotropy is not evident except in the lowermost few hundred kilometers of the mantle, where there is evidence of transversely isotropic (radially anisotropic) material, in which $V_{SH} > V_{SV}$, with significant lateral variations in the magnitude of the anisotropy (Kendall and Silver 1996, Matzel et al. 1996, Garnero and Lay 1997). The possibility of some weak radial anisotropy in the uppermost lower mantle (660-1000 km), in which $V_{SV} > V_{SH}$, has also been suggested (Montagner and Kennett 1996) from modeling of normal modes.

Mineralogical interpretation

The apparent isotropy of the bulk of the lower mantle is somewhat puzzling, given that magnesiowüstite and silicate perovskite, the minerals believed to comprise the bulk of the lower mantle, both exhibit elastic anisotropy (Hemley and Cohen 1996, Karato 1997) and, given what is currently known about the pressure- and temperature-dependence of the relevant elastic moduli (Karato 1998a), should do so through most of the lower mantle. Macroscopic seismic expression of such anisotropy, however, would require preferred orientation of anisotropic crystals (Fig. 7b). Thus, the absence of

seismic anisotropy in the lower mantle suggests that the minerals assemblages therein do not develop lattice preferred orientation (LPO). While at least portions of the upper mantle appear to deform via a dislocation creep mechanism (Karato and Wu 1993), the conditions of stress and grain size in the lower mantle may fall within the regime governed by the diffusion creep mechanism (Karato 1998a), in which LPO fabrics do not form. Any local or regional deviations from this isotropy might then arise from corresponding regional variations in stress or grain size, reflecting lateral variations in composition, mineralogy, temperature, or deformation history. On the other hand, lower mantle minerals may fail to develop LPO even when deformed within the dislocation creep regime, a hypothesis suggested by deformation experiments on magnesium silicate perovskite (Meade et al. 1995)

Mantle flow. While lithospheric anisotropy is commonly interpreted in terms of preferred orientation of olivine fabrics reflecting spreading or mantle flow (Ribe 1989, Russo et al. 1996), mineralogical interpretation of any limited anisotropy in the deep mantle is still in its infancy. Anderson (1989b) suggested that LPO of silicate ilmenite in subducting slabs could contribute some anisotropy to areas of the topmost lower mantle. Karato (1998a, 1998d) recently used a numerical method (Montagner and Nataf 1986) to calculate the effective elastic moduli arising from lattice preferred orientation in lower mantle mineral assemblages, incorporating current estimates of the significant pressure- and temperature-dependence of mineral anisotropy (Isaak et al. 1990, Karki et al. 1997a, 1997b). Invoking the relative magnitudes of V_{SH} and V_{SV} as observed along certain source-receiver paths, he proposed interpretation of narrow anisotropic layers at the top and bottom of the lower mantle in terms of LPO induced by horizontal flow. In addition to LPO of anisotropic crystals, however, radial anisotropy can also arise from shape preferred orientation (SPO) of aligned inclusions of distinct elastic properties (Fig. 7b). Because observation of $V_{SH} > V_{SV}$ at the core-mantle boundary is consistent with effective horizontal layering, Karato (1998a) interpreted this as due to horizontally aligned SPO. Given the large differences in shear moduli between silicate perovskite and magnesiowüstite, either inclusions of one in the other or inclusions of melt in an aggregate could satisfy the requirements of such SPO.

ANELASTIC ATTENUATION AND VISCOSITY

Geophysical background

Thus far we have considered the elastic properties of the mantle, but the mantle is not perfectly elastic (Weidner this volume). Furthermore, neglect of anelastic effects when inverting seismic data can significantly affect velocity gradients and fine structure in the resulting models (Kennett 1975, Karato 1993).

Attenuation. Anelasticity at the frequency of seismic waves is often described by a "quality factor" Q, where the "attenuation" Q^{-1} describes the fractional energy loss per oscillation. Attenuation can be measured by examining the amplitude decay of body waves, such as S- and P-waves reflected one or more times from the core. However, even in the absence of anelastic attenuation, the amplitudes of body waves decay due to simple geometrical spreading of the wavefronts, so this effect first must be accounted for in order to estimate any anelastic attenuation. Since geometrical spreading will be significantly affected by the presence of lateral velocity variations, there is an inherent trade-off between resolving heterogeneity and attenuation (Bhattacharyya et al. 1996, Bhattacharyya 1998). Normal modes of free oscillation (Fig. 8a), in which the earth undergoes spheroidal and toroidal deformations, can also be used to measure anelastic attenuation. The effects of attenuation are evident both in the quality factors for the amplitudes of individual modes (e.g. CORE11 of Widmer et al. 1993) and in the velocity dispersion (frequency-dependence of velocities, Fig. 8b) which must attend any finite Q (Montagner

and Kennett 1996), both of which can be determined from the spreading of spectral peaks (Durek and Ekström 1997). While fundamental modes possess low resolution in the lower mantle, the use of higher-order overtone modes (Okal and Jo 1990) can markedly improve models of this region. However, spectral peak spreading also accompanies velocity heterogeneity, so again there is an inherent trade-off between resolution of lateral heterogeneity and anelasticity (Romanowicz 1987).

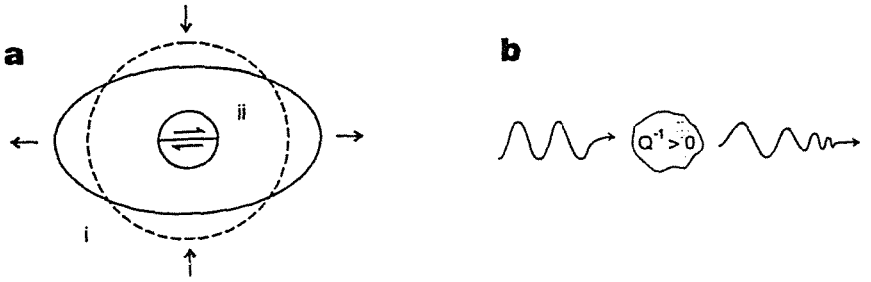

Figure 8. Anelasticity: Normal modes of free oscillation (a) may be spheroidal (i) or toroidal (ii). Attenuation of seismic waves (b) results in both a decrease in amplitude and a dispersion of high- and low-frequency components.

Attenuation can occur either in bulk (isotropic volume changes) or in shear (isochoric deformation) strain, measured by Q_κ and Q_μ, respectively. Because there are few data that constrain the former, and because most attenuation mechanisms operate largely in shear, Q_κ is often assumed to be infinite (Q_κ^{-1} is zero) while normal mode data are inverted for radial models of Q_μ (Montagner and Kennett 1996). Bulk and shear attenuation can be mapped directly into quality factors for V_P and V_S, given by Q_P and Q_S, respectively:

$$Q_S^{-1} = Q_\mu^{-1} \quad , \quad Q_P^{-1} = LQ_\mu^{-1} + (1 - L)Q_\kappa^{-1} \quad , \quad L \equiv \tfrac{4}{3}(V_S / V_P)^2$$

In many radial models of attenuation, Q increases with depth. However, the magnitude and even the sign of the lower mantle Q_μ gradient exhibits significant dependence upon choice of starting model (Montagner and Kennett 1996). What does seem clear is that Q_μ in the lower mantle (> 400) exceeds that in the upper mantle (< 200).

While attenuation observed in the laboratory usually varies with frequency, most seismological models assume that Q is independent of frequency, and the fact that such models can satisfy available data attests to the poor resolving power of current models of anelasticity (Anderson 1989b). Evidence of frequency dependence of Q can be found in the observation that, over the range of frequencies characteristic of body waves, energy at higher frequencies is attenuated more strongly than at lower frequencies. Furthermore, Q at the lower frequencies of normal modes cannot be simply extrapolated to even lower tidal frequencies. Moreover, the frequency dependence of Q varies with depth. In the lower mantle, body waves are attenuated less strongly than are longer-period (i.e. lower-frequency) normal modes. In the upper mantle and in the bottommost lower mantle, on the other hand, strong attenuation extends to higher frequencies. Such observations suggest the presence of a high-frequency cut-off (Sipkin and Jordan 1979), leading to a model of an "absorption band" for Q whose frequency limits shift with pressure and temperature and hence with depth (Anderson and Given 1982).

Above and beyond such changes in Q with depth, lateral variations in Q can amount to 50-100%. Thus, 1-D models of attenuation are fundamentally unsatisfactory, especially given the dependence of inversions for velocity structure upon accurate representation of Q structure (Montagner and Kennett 1996). While 3-D models of Q are now beginning to emerge (Romanowicz 1994, 1998), they are still generally based on the assumption of frequency-independence. Complicating such efforts are the effects of lateral heterogeneity, because scattering of energy off of heterogeneities can also result in significant apparent attenuation of seismic energy. Attempts at distinguishing intrinsic attenuation from such scattering are best undertaken at low frequencies, so that small scatterers have minimal effect, but this limits potential spatial resolution.

Viscosity. While anelasticity at seismic frequencies appears as attenuation, anelastic behavior at much longer periods manifests itself in the form of viscosity ν. Radial viscosity models are generally constructed from one or both of two data sets. The first data set consists of records of sea-level changes associated with post-glacial rebound of the lithosphere, and these data constrain the absolute value of mantle viscosity (Haskell 1935, 1936; Fang and Hager 1996). The second method is somewhat more complicated and constrains only relative viscosity changes (King 1995, Forte and Mitrovica 1996). Viscosity models are constructed so that the gravity-driven flow induced by a specified 2- or 3-D distribution of density heterogeneities in the mantle will generate dynamic topography that reproduces observed long-wavelength geoid anomalies (Hager et al. 1985, Forte and Woodward 1997). Further constraints are sometimes imposed based upon observed plate velocities (Lithgow-Bertelloni and Richards 1998). In addition to geoid observations, the second method requires as data a model of mantle density heterogeneity. This is usually constructed by taking a tomographic image of mantle seismic velocities and mapping it into an image of densities using empirical depth-dependent scaling functions between density and velocity (Hager et al. 1985, Kido and Čadek 1997), thereby assuming that all lateral velocity variations arise solely from lateral variations in temperature rather than chemistry. In terms of elastic moduli, this amounts to assuming values for ratios of temperature derivatives at constant pressure and composition:

$$\left(\frac{\partial \ln \rho}{\partial \ln V_\phi}\right)_{P,X} = \frac{-2}{(1 - \delta_S)} \quad , \quad \left(\frac{\partial \ln \rho}{\partial \ln V_S}\right)_{P,X} = \frac{-2}{(1 - \zeta)}$$

where δ_S and ζ were defined above.

The results of such inversions are non-unique, possess poorer resolution in the lower than in the upper mantle, and exhibit dependence upon choice of starting model (King and Masters 1992, King 1995, Mitrovica 1996). However, they generally indicate a viscosity increase of about an order of magnitude in the upper part of the lower mantle, and they suggest the possibility of a narrow zone of low viscosity in the topmost lower mantle (Hager and Richards 1989, King 1995, Mitrovica 1996, Kido and Čadek 1997). While the resolving power of post-glacial rebound studies drops off rapidly with depth in the lower mantle, such data have been reconciled with long-wavelength geoid analyses. Both data sets can be fit with models which exhibit a viscosity jump at 1000 km (Forte and Mitrovica 1996). This viscosity transition however, could also be a smooth gradient, because the limited resolution of the inversion and of the tomographic models does not allow fine structure to be reliably distinguished (Kido and Čadek 1997). The largest uncertainties in such analyses may arise from their implicit assumption that there are no lateral viscosity variations. Just as in the case of attenuation, such lateral variations in viscosity may in fact be extremely large, changing by orders of magnitude in response to temperature anomalies of hundreds of degrees. Such changes could significantly impact the simple flow models derived under the assumption of lateral homogeneity, requiring changes in the inverted viscosity structure in order to fit the geoid observations. Recent

studies of the impact of lateral viscosity variations upon geoid calculations, however, have thus far revealed only second-order effects (Ravine and Phipps Morgan 1993, Zhang and Christensen 1993, Zhang and Yuen 1995).

Mineralogical interpretation

Karato (1998b) has proposed a theory to distinguish mechanistically between short-term and long-term rheology, in which the elastic deformation of seismic wave attenuation arises from "micro-glide" migration of geometrical kinks while the transient and steady-state creep associated with viscosity arises from "macro-glide" continuing nucleation of kinks. He has also suggested (Karato 1998c) that the shorter time scales of post-glacial rebound may result in smaller effective viscosities relative to processes of mantle convection, due to a transition from inter-granular creep to steady-state creep at the high strains of mantle convection.

Attenuation. Seismic attenuation, Q^{-1}, in minerals can be a complicated function of temperature, pressure, stress, frequency, grain size, and water content (Anderson 1989b, Karato 1998b, Karato and Jung 1998, Jackson 1998b). In the lower mantle, low values of Q_S may indicate that the rheology thereof is controlled by the magnesiowüstite phase, which is weaker than the presumably more abundant silicate perovskite phase (Getting et al. 1997). Very low values of Q_S, on the other hand, would be suggestive of local melting (Williams and Garnero 1996). However, few inferences regarding chemical composition of the lower mantle can currently be drawn from Q models with confidence. Perhaps the greatest utility of imaging radial and lateral variations in mantle attenuation lies in its potential for resolving the ambiguities in the thermal and compositional origin of velocity anomalies as imaged by seismic tomography (Romanowicz 1997). Since attenuation is so much more sensitive to temperature than is velocity, any tomographic low-velocity anomalies that are not accompanied by high local attenuation may be suspected of having compositional components instead of being purely thermal in nature.

Viscosity. As for the ratios of the partial derivatives of density and velocity with respect to temperature, used in extracting viscosity models from the long-wavelength geoid as described above, for most minerals δ_S is 5 ± 2 and ζ is 6 ± 2 (Anderson 1989b) near the top of the lower mantle, in reasonable agreement with the magnitudes of the density-velocity scaling functions commonly employed (Kido and Čadek 1997). However, if δ_S actually falls slightly with depth (Anderson 1998) then the ratio of partial derivatives should increase with depth, rather than decreasing or remaining constant as is sometimes assumed (Kido and Čadek 1997).

The issue of lower mantle viscosity also raises the question of the effective viscosity of mineral aggregates. In particular, as noted above, magnesiowüstite appears to be significantly weaker than silicate perovskite under lower mantle conditions. Although perovskite should be the more abundant phase, it is not clear which phase will control the aggregate lower mantle viscosity, because this depends upon the unknown geometry adopted by the weaker phase during deformation (Karato 1997).

Just as with attenuation, the strong temperature dependence of viscosity may prove useful in resolving temperature-composition trade-offs in images of density or velocity anomalies. Viscosity variations may also provide evidence of effects of phase transformations on rheology. Proximity to phase changes which involve softening of lattice vibrational modes can result in enhanced creep and thus lower viscosity (Poirier 1981, Rubie and Brearley 1994, Karato 1997). In slab and plume material, latent heat release from material undergoing exothermic transitions can result in locally low viscosities (Karato 1997, Bina 1998b), as can weakening due to grain size reduction which may accompany phase transitions at low temperature (Karato and Li 1992, Karato 1997).

Indeed, the issue of grain size provide a potential link between mantle viscosity and anisotropy. A local reduction in grain size that leads to diffusion creep and an absence of LPO anisotropy might also be expected to induce rheological weakening and consequent locally low viscosities.

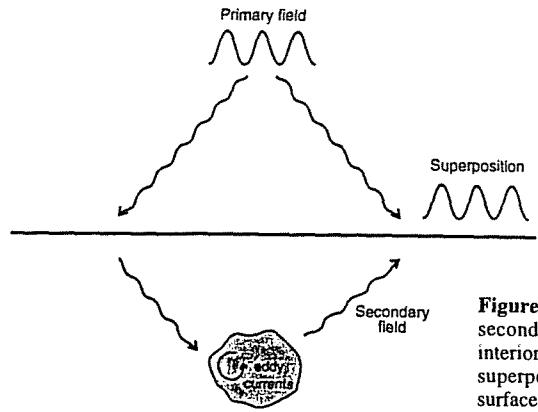

Figure 9. Changing external magnetic fields induce secondary eddy currents in the earth's conductive interior, generating secondary magnetic fields that are superposed upon the external inducing field at the surface.

ELECTRICAL CONDUCTIVITY

Geophysical background

Electrical conductivity in the earth is measured by studying the frequency-dependent electromagnetic response (Roberts 1986) represented by temporal variations in the geomagnetic field. Such temporal variations in external magnetic fields induce secondary eddy currents within conductive pathways in the earth's interior (Fig. 9), and the superposition upon the external inducing field of the secondary magnetic fields generated by these eddy currents can be observed at the surface (Schultz and Larsen 1987). Variations with periods of less than a year arise from solar-atmospheric interactions, inducing consequent telluric currents in the earth, and constrain average conductivity to depths of about 1500 km. Below this depth in the lower mantle, longer period variations in the geomagnetic field, such as the spectrum of secular variation presumably arising from core-mantle interactions or the variations caused by the sunspot cycle, must be used to constrain conductivity (Bott 1982). Inversion of such data suffers from the usual non-uniqueness of the resulting models, but one robust result appears to be that electrical conductivity increases by 1 or 2 orders of magnitude from the upper to the lower mantle. Furthermore, electrical conductivity increases with depth in the lower mantle by about an order of magnitude (from ~1 to ~10 S/m) from top to bottom (Shankland et al. 1993, Petersons and Constable 1996, Honkura et al. 1996). Finally, additional constraints upon electrical conductivity in the lowermost mantle can be inferred from such rotational effects of electromagnetic stresses across the core-mantle boundary as length-of-day variations (Stewart et al. 1995) and nutation of the earth's polar axis (Buffett et al. 1997). The magnitude of the increase in electrical conductivity near the core-mantle boundary remains a matter of debate, because inversions directly constrain conductance rather than conductivity. Because thickness of the highly conductive layer is poorly constrained, the length-of-day constraints on the electromagnetic torque between core and lowermost mantle can be satisfied if the bottom few hundred kilometers of the mantle have a conductivity of 100-1000 S/m (Stewart et al. 1995), but a thinner layer of even higher conductivity is also possible.

Radial profiles of electrical conductivity have been studied for some time (Lahiri and Price 1939). Nonetheless, it is clear that electrical conductivity in the earth exhibits significant lateral heterogeneity (Schultz 1990, Schultz and Larsen 1990). Recently constructed 3-D inverse models (Schultz and Pritchard 1995, 1998) suggest, however, that lateral heterogeneity in the lower mantle may be less extreme than the order of magnitude variations seen in the upper mantle. As in the case of seismic tomography, electromagnetic data are most sensitive to bulk electrical properties rather than to sharp interfaces (Everett and Schultz 1996). Evidence of persistent, long-wavelength, lateral heterogeneity in the geomagnetic field may be attributable either to thermal anomalies or to local regions of high electrical conductivity in the lower mantle (Gubbins 1988, 1994; Johnson and Constable 1998). Thus, mantle compositional heterogeneity may be mapped through electrical as well as seismic methods (Johnson and Constable 1997, Forsyth et al. 1998), especially if thermal anomalies can be independently identified through anelastic effects.

Mineralogical interpretation

While some have suggested bulk iron-enrichment of the lower mantle to account for conductivity increases (Li and Jeanloz 1991a), others have argued that they are due to intrinsic effects of high pressures and temperatures on lower mantle silicates (Peyronneau and Poirier 1989, Shankland et al. 1993). In general, such changes in electrical conductivity are probably controlled by interplay between oxygen fugacity, volatiles (e.g. CO_2, H_2O), and compositional (e.g. ferric iron) variations (Li et al. 1993). If, for example, Fe^{3+} can be accommodated at low levels within the most abundant phases, then the activity of the ferric component will remain low and so will the fugacity of oxygen (f_{O_2}). On the other hand, if Fe^{3+} can be accommodated only within minor secondary phases, the concentration and activity of the ferric components will be high, driving up the f_{O_2}.

In the upper mantle, between 200 and 300 km depth, oxygen fugacity falls to the point where carbonates are reduced to diamond, and the moderate solubility of ferric iron in transition zone minerals suggests that f_{O_2} should continue to fall at greater depths (Wood et al. 1996). Indeed, recent work (Woodland and Angel 1998) demonstrates significant stability of ferric iron in the wadsleyite (β-phase) structure, implying a low oxygen fugacity in the transition zone. Recent observations of extensive ferric iron solubility in aluminous silicate perovskite (Wood and Rubie 1996, McCammon 1997) support the continuation of such low oxygen fugacities and diamond stability into the lower mantle, thus allowing the electrical conductivity in this region to be controlled by the dominant perovskite phase. This is in contrast to earlier suggestions (Wood et al. 1996), based upon a presumed low iron solubility in perovskite, that concentration of iron in the magnesiowüstite phase should lead to increased oxygen fugacity and a return to carbonate stability. This latter scenario would have awkwardly required that the electrical conductivity of the lower mantle be controlled by the secondary magnesiowüstite phase, but the revelation of significant Fe^{3+} solubility in silicate perovskite supports the simpler scenario in which the primary perovskite phase controls the bulk electrical conductivity. Moreover, additional recent work (Mao et al. 1997) suggests that iron-magnesium partitioning between these two lower mantle phases is dependent upon pressure, temperature, and composition, implying that the iron content of silicate perovskite should increase substantially with depth, presumably leading to concomitant electrical conductivity increases. Other studies, however, have found no such systematic depth dependence of Fe-Mg partitioning (Kesson et al. 1998).

Water may also play a role in controlling electrical conductivity (Karato 1990, Li and Jeanloz 1991b), with any H_2O entering the lower mantle from the transition zone in the form of hydrous phases residing in subducting lithosphere (Bose and Navrotsky 1998, Navrotsky this volume). The Fe-Al coupling noted above, however, remains important.

The solubility of H in stishovite rises with increasing Al substitution (Pawley et al. 1993), and the solubility of H in ferromagnesian silicate perovskite may also increase with increasing Fe and Al substitution (Meade et al. 1994). However, the apparent absence of broadened seismic discontinuities in the transition zone (Wood 1995) and the absence of OH in olivine and orthopyroxene inclusions from diamonds (McMillan et al. 1996) suggest that the H_2O content of the transition zone and lower mantle may be generally quite low.

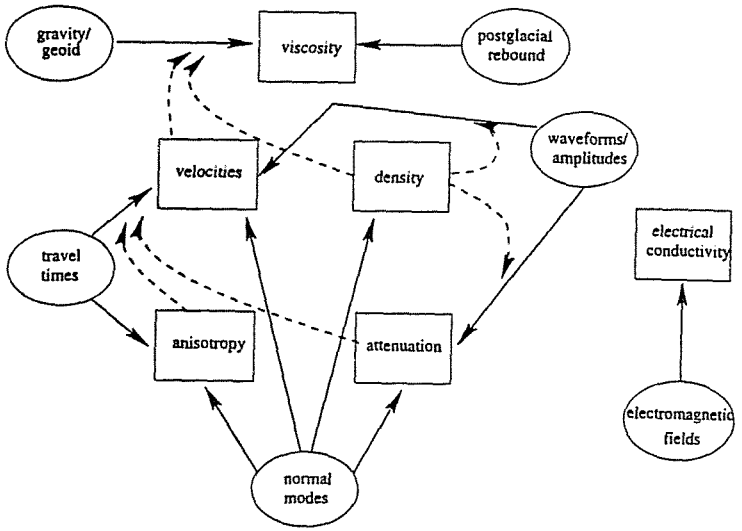

Figure 10. Schematic flowchart illustrating geophysical observations (ovals) and the deep mantle properties which they constrain (rectangles). Solid arrows indicate directions of constraints; dotted arrows show secondary feedback constraints.

CONCLUDING REMARKS

In constructing models of properties of the deep mantle, there is considerable interplay between various geophysical constraints (Fig. 10). The travel times of seismic waves, of course, serve to constrain velocity structure and velocity anisotropy. Normal modes of oscillation, while they also constrain velocities and anisotropy, further serve to constrain the structure of density and anelastic attenuation. The amplitudes of waveforms also constrain velocities and attenuation. On the other hand, both gravity anomalies expressed in the geoid and sea level changes associated with post-glacial rebound combine to constrain viscosity structure. Electromagnetic field variations constrain deep electrical conductivity. Several of the constraints provided by these observations, however, involve significant feedback. Information on the structure of attenuation and anisotropy can significantly affect the determination of velocity structure, for example. Furthermore, models of density are required in order to extract information on velocities and attenuation from the amplitudes of waveforms, and both density and laterally heterogeneous velocity models are necessary in order to constrain viscosity structure from the long-wavelength geoid.

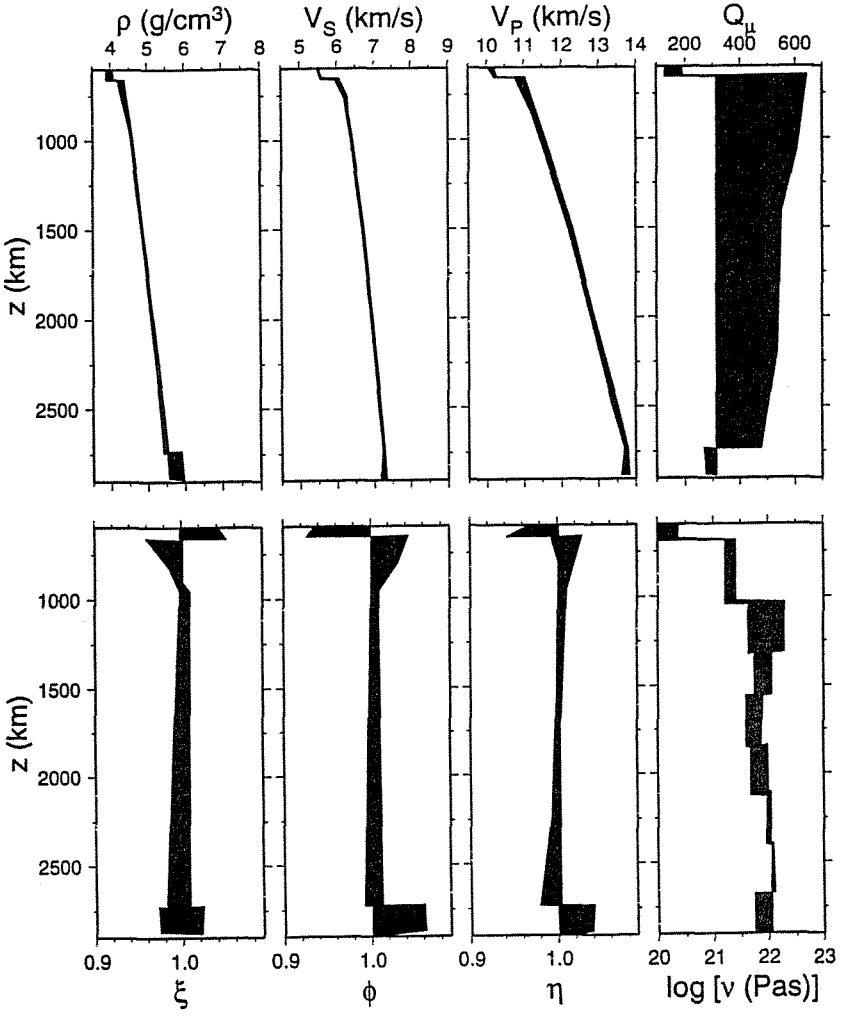

Figure 11. Ranges of lower mantle properties as constrained by inverse models of geophysical observations: density (ρ), seismic wave velocities (S-wave V_S, P-wave V_P) shear quality factor (Q_μ, inverse of shear anelastic attenuation), radial anisotropy (P-wave ϕ, S-wave ξ, off-axis η), logarithm of viscosity (ν), assembled from results of Montagner and Kennett (1996) and Forte and Mitrovica (1996).

Such geophysical models (Fig. 11) provide a variety of constraints upon lower mantle physical conditions. Seismic velocities, density, and electrical conductivity all depend upon temperature as well as upon composition and mineralogy, with electrical conductivity being particularly sensitive to oxygen fugacity through its effects upon ferric iron content. Elastic anisotropy also depends upon temperature and composition, but this property is also sensitive to strain and to grain size. The ambiguity between thermal and compositional origins for lower mantle geophysical anomalies can be investigated through study of anelastic properties, in the form of viscosity and seismic wave attenuation. Both of these properties, while also sensitive to stress, grain size, and composition (especially volatile content), are strongly dependent upon temperature, so that a thermal origin for

deep mantle anomalies should have a strong anelastic signature. Resolution of this thermal-compositional ambiguity will also be facilitated by improved equations of state for shear moduli at high temperatures and pressures, because this will allow more thorough analysis of whether coupled variations in P- and S-wave velocities (i.e. Poisson's ratio) are consistent with isochemical thermal perturbations. Thermal anomalies also will generate buoyancy anomalies which should be consistent with the dynamics of mantle flow.

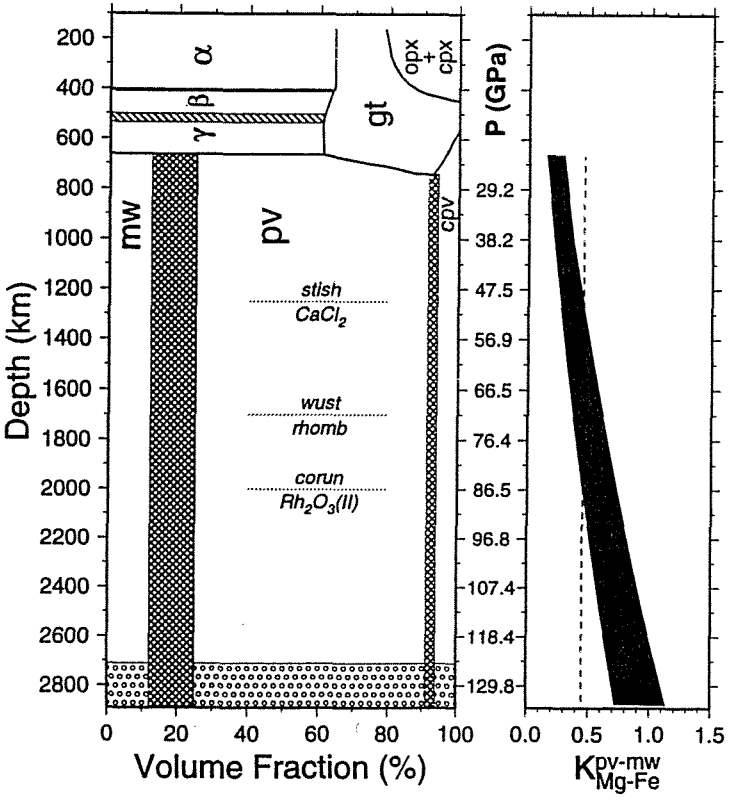

Figure 12. Schematic diagram (after the style of Ringwood 1989) of relative mineral proportions in the mantle (left). Phases are olivine (α), wadsleyite (β), ringwoodite (γ), ortho- and clinopyroxene (opx+cpx), garnet-majorite (gt), magnesiowüstite (mw), ferromagnesian silicate perovskite (pv), and calcium silicate perovskite (cpv). Hatched regions indicate divariant phase transitions in olivine polymorphs. Crosshatched zones denote uncertainty in phase proportions of mw and cpv. Dotted lines indicate approximate pressures of oxide transitions. Also shown (right) is range (shaded region) of partitioning coefficient (K_{Mg-Fe}^{pv-mw}) of Mao et al. (1997) for best-fit lower mantle compositions computed herein and constant value (dashed line) adopted by Kesson et al. (1998).

For a lower mantle composed primarily of silicate perovskite and magnesiowüstite (Fig. 12), current data do not appear to require significant enrichment in iron or silica relative to a pyrolitic upper mantle. However, the dependence of elastic properties upon calcium, aluminum, and ferric iron content has not yet been fully incorporated into such analyses, and both the uppermost and lowermost portions of the lower mantle deviate significantly from this simple model. Coupled solubility of aluminum and ferric iron in silicate perovskite may permit coexistence of garnet and silicate perovskite throughout the

uppermost ~100 km of the lower mantle (Wood and Rubie 1996), while γ silicate spinel (ringwoodite) disproportionates to silicate perovskite and magnesiowüstite over a much narrower depth interval (Akaogi et al. 1998).

Beneath cold subduction zones, the disappearance of ringwoodite may be depressed by several tens of kilometers (Bina and Helffrich 1994), and at very low temperatures (below 1000 K) ringwoodite may briefly transform to magnesiowüstite and stishovite before subsequently forming silicate perovskite and magnesiowüstite (Akaogi et al. 1998). As for the transition between garnet and silicate perovskite in the uppermost lower mantle, this may be interrupted by a broad region of stability for silicate ilmenite (Anderson 1989b, Reynard et al. 1996, Reynard and Rubie 1996, Irifune et al. 1996, Vacher et al. 1998) before eventual formation of silicate perovskite.

Despite the apparent absence of major seismic velocity discontinuities of global extent in the lower mantle, additional phase changes may play a role in lower mantle properties (Fig. 12). Lateral variations in temperature or Fe/Mg ratio, for example, may cause local breakdown of silicate perovskite to mixed oxides (Wang et al. 1997). With regard to the oxides, FeO undergoes transformation to a rhombohedral structure at pressures corresponding to ~1700 km (Mao et al. 1996), perhaps shifting to shallower depths in (Mg,Fe)O magnesiowüstite. Furthermore, SiO_2 transforms from stishovite to a $CaCl_2$ structure at pressures corresponding to those at ~1250 km (Tsuchida and Yagi 1989, Kingma et al. 1995). Finally, Al_2O_3 transforms from corundum to a Rh_2O_3(II) structure at pressures corresponding to ~2000 km (Marton and Cohen 1994, Funamori and Jeanloz 1997), with potential consequences for stability, elasticity, elemental partitioning, and buffering of oxygen fugacity in phases such as ferromagnesian silicate perovskite in which alumina exhibits significant solubility.

ACKNOWLEDGMENTS

I thank Michael Hedlin, George Helffrich, Rus Hemley, Catherine Johnson, Scott King, Fred Marton, Emile Okal, Paul Silver, Fumiko Tajima, Rob van der Hilst, and Doug Wiens for helpful comments. I acknowledge the support of NSF grant INT-9603234. Figures 1, 6, 7a, 8, and 9 were drafted by Eric Yates and Figures 7b and 10 by Fred Marton.

REFERENCES

Akaogi M, Kojitani H, Matsuzaka K, Suzuki T (1998) Postspinel transformations in the system Mg_2SiO_4-Fe_2SiO_4: Element partitioning, calorimetry, and thermodynamic calculation. *In:* MH Manghnani, T Yagi (eds) Properties of Earth and Planetary Materials at High Pressure and Temperature p 373-384 American Geophysical Union, Washington, DC

Anders E, Grevesse N (1989) Abundance of the elements: Meteoritic and solar. Geochim Cosmochim Acta 53:197-214

Anderson DL, Given JW (1982) Absorption band Q model for the Earth. J Geophys Res 87:3893-3904

Anderson DL (1989a) Composition of the Earth. Science 243:367-370

Anderson DL (1989b) Theory of the Earth. Blackwell, Boston

Anderson OL (1998) Thermoelastic properties of $MgSiO_3$ perovskite using the Debye approach. Am Mineral 83:23-35

Ando M (1984) ScS polarization anisotropy around the Pacific ocean. J Phys Earth 32:179-196

Astiz L, Earle PS, Shearer PM (1996) Global stacking of broadband seismograms. Seismo Res Lett 67:8-18

Babuska V, Cara M (1991) Seismic Anisotropy in the Earth. Kluwer, Dordrecht

Beckford W (1786) Vathek. Reprinted by Ballantine, New York, 1971

Bell PM, Mao HK, Xu JA (1987) Error analysis of parameter-fitting in equations of state for mantle minerals. *In:* MH Manghnani, Y Syono (eds) High-Pressure Research in Mineral Physics, p 447-454 Terra, Tokyo

Bhattacharyya J (1998) Investigation of biasing factors in the measurement of body wave attenuation in the mantle using long-period waveforms. Pure Appl Geoph (in press)

Bhattacharyya J, Masters G, Shearer P (1996) Global variations of shear wave attenuation in the upper mantle. J Geophys Res 101:22273-22289

Biémont E, Baudoux M, Kurucz RL, Ansbacher W, Pinnington EH (1991) The solar abundance of iron: A "final" word! Astron Astrophys 249:539-544

Bina CR (1995) Confidence limits for silicate perovskite equations of state. Phys Chem Min 22:375-382

Bina CR (1998a) Free energy minimization by simulated annealing with applications to lithospheric slabs and mantle plumes. Pure Appl Geophys 151:605-618

Bina CR (1998b) A note on metastable latent heat release in deep seismogenesis. Earth Planets Space (submitted)

Bina CR, Helffrich GR (1992) Calculation of elastic properties from thermodynamic equation of state principles. Ann Rev Earth Planet Sci 20:527-552

Bina CR, Helffrich G (1994) Phase transition Clapeyron slopes and transition zone seismic discontinuity topography. J Geophys Res 99:15853-15860

Bina CR, Kumazawa M (1993) Thermodynamic coupling of phase and chemical boundaries in planetary interiors. Phys Earth Planet Inter 76:329-341

Bina CR, Silver PG (1997) Bulk sound travel times and implications for mantle composition and outer core heterogeneity. Geophys Res Lett 24:499-502

Birch F (1952) Elasticity and constitution of the Earth's interior. J Geophys Res 57:227-286

Bolton H, Masters G (1996) A region of anomalous d ln V_S/d ln V_P in the deep mantle. Eos Trans Am Geophys Union 77:F697

Bose K, Navrotsky A (1998) Thermochemistry and phase equilibria of hydrous phases in the system MgO-SiO_2-H_2O: Implications for volatile transport to the mantle. J Geophys Res 103:9713-9719

Bott MHP (1982) The Interior of the Earth. Elsevier, New York

Buffett BA, Herring TA, Mathews PM (1997) New constraints on the structure of the core-mantle boundary from observations of the Earth's nutations. Eos Trans Am Geophys Union 78:F2

Bukowinski MST, Wolf GH (1990) Thermodynamically consistent decompression: Implications for lower mantle composition. J Geophys Res 95:12583-12593

Byerley P (1926) The Montana earthquake of June 28, 1925. Bull Seis Soc Am 16:209-265

Castle JC (1998) Imaging mid-mantle discontinuities: Implications for mantle chemistry, dynamics, rheology, and deep earthquakes. PhD dissertation, University of Washington, Seattle

Christensen NI, Crosson RS (1968) Seismic anisotropy in the upper mantle. Tectonophys 6:93-107

Clarke, TJ (1993) The complete ordered ray expansion 2: Multi-phase body wave tomography. Geophys J Int'l 115:435-444

Crampin S (1984) An introduction to wave propagation in anisotropic media. Geophys J R Astr Soc 76:17-28

Cummins PR, Takeuchi N, Geller RJ (1997) Computation of complete synthetic seismograms from laterally heterogeneous models using the Direct Solution Method. Geophys J Int'l 130:1-16

Davies GF (1990) Mantle plumes, mantle stirring, and hotspot chemistry. Earth Planet Sci Lett 99:94-109

Durek JJ, Ekström G (1997) Investigating discrepancies among measurements of traveling and standing wave attenuation. J Geophys Res 102:24529-24544

Dziewonski AM, Anderson DL (1981) Preliminary reference Earth model. Phys Earth Planet Inter 25:297-356

Everett ME, Schultz A (1996) Geomagnetic induction in a heterogeneous sphere: Azimuthally symmetric test computations and the response of an undulating 660-km discontinuity. J Geophys Res 101:2765-2783

Fabrichnaya OB (1995) Thermodynamic data for phases in the FeO-MgO-SiO_2 system and phase relations in the mantle transition zone. Phys Chem Min 22:323-332

Fang M, Hager BH (1996) The sensitivity of post-glacial sea level to viscosity structure and ice-load history for realistically parameterized viscosity profiles. Geophys Res Lett 23:3787-3790

Fei Y, Wang Y, Finger LW (1996) Maximum solubility of FeO in (Mg, Fe)SiO_3-perovskite as a function of temperature at 26 GPa: Implication for FeO content in the lower mantle. J Geophys Res 101:11525-11530

Fischer KM, Wiens DA (1996) The depth distribution of mantle anisotropy beneath the Tonga subduction zone. Earth Planet Sci Lett 142:253-260

Forsyth DW, Scheirer DS, Webb SC, Dorman LM, Orcutt JA, Harding AJ, Blackman DK, Phipps Morgan J, Detrick RS, Shen Y, Wolfe CJ, Canales JP, Toomey DR, Sheehan AF, Solomon SC, Wilcock WSD (1998) Imaging the deep seismic structure beneath a mid-ocean ridge: The MELT experiment. Science 280:1215-1218

Forte AM, Mitrovica JX (1996) New inferences of mantle viscosity from joint inversion of long-wavelength mantle convection and post-glacial rebound data. Geophys Res Lett 23:1147-1150

Forte AM, Woodward RL (1997) Seismic-geodynamic constraints on three-dimensional structure, vertical flow, and heat transfer in the mantle. J Geophys Res 102:17981-17994

Fouch MJ, Fischer KM (1996) Mantle anisotropy beneath northwest Pacific subduction zones. J Geophys Res 101:15987-16002

Fukao Y (1984) Evidence from core-reflected shear waves for anisotropy in the Earth's mantle. Nature 309:695-698

Fukao Y, Obayashi M, Inoue H, Nenbai M (1992) Subducting slabs stagnant in the mantle transition zone. J Geophys Res 97:4809-4822
Funamori N, Jeanloz R (1997) High-pressure transformation of Al_2O_3. Science 278:1109-1111
Garlick GD (1969) Consequences of chemical equilibrium across phase changes in the mantle. Lithos 2:325-331
Garnero EJ, Grand SP, Helmberger DV (1993) Low P-wave velocity at the base of the mantle. Geophys Res Lett 17:1843-1846
Garnero EJ, Lay T (1997) Lateral variation in lowermost mantle shear wave anisotropy beneath the north Pacific and Alaska, J Geophys Res 102:8121-8136
Geller RJ, Hara T (1993) Two efficient algorithms for iterative linearized inversion of seismic waveform data. Geophys J Int'l 115:699-710
Getting IC, Dutton SJ, Burnley PC, Karato S, Spetzler HA (1997) Shear attenuation and dispersion in MgO. Phys Earth Planet Inter 99:249-257
Gilbert JF, Dziewonski AM (1975) An application of normal mode theory to the retrieval of structure parameters and source mechanism from seismic spectra. Phil Trans R Soc Lond A278:187-269
Grand SP (1994) Mantle shear structure beneath the Americas and surrounding oceans. J Geophys Res 99:11591-11621
Grand SP, Helmberger DV (1984) Upper mantle shear structure of North America. Geophys J R Astr Soc 76:399-438
Grand SP, van der Hilst RD, Widiyantoro S (1997) Global seismic tomography: Snapshot of convection in the Earth. Geol Soc Am Today 7(4):1-7
Gubbins D (1988) Thermal core-mantle interactions and the time-averaged palaeomagnetic field. J Geophys Res 93:3413-3420
Gubbins D (1994) Geomagnetic polarity reversals: A connection with secular variation and core-mantle interaction? Rev Geophys 32:61-83
Gudmundsson O, Davis JH, Clayton RW (1990) Stochastic analysis of global traveltime data: Mantle heterogeneity and random errors in the ISC data. Geophys J Int'l 102:25-43
Hager BH, Clayton RW, Richards MA, Comer RP, Dziewonski AM (1985) Lower mantle heterogeneity, dynamic topography and the geoid. Nature 313:541-545
Hager BH, Richards MA (1989) Long-wavelength variations in Earth's geoid: physical models and dynamical implications. Phil Trans R Soc Lond A328:309-327
Hart S, Zindler A (1989) Constraints on the nature and development of chemical heterogeneities in the mantle. *In:* WR Peltier (ed) Mantle Convection: Plate Tectonics and Global Dynamics p 261-387 Gordon and Breach, New York
Harte B, Harris JW (1994) Lower mantle associations preserved in diamonds. Mineral Mag 58A:384-385
Harte B, Hutchison MT, Harris JW (1994) Trace element characteristics of the lower mantle: An ion probe study of inclusions in diamonds from São Luiz, Brazil. Mineral Mag 58A:386-387
Haskell NA (1935) The motion of a fluid under a surface load, I. Physics 6:265-269
Haskell NA (1936) The motion of a fluid under a surface load, II. Physics 7:56-61
Hedlin MAH, Shearer PM, Earle PS (1997) Seismic evidence for small-scale heterogeneity throughout the Earth's mantle. Nature 387:145-150
Helffrich G, Bina CR (1994) Frequency dependence of the visibility and depths of mantle seismic discontinuities. Geophys Res Lett 21:2613-2616
Helffrich GR, Wood BJ (1996) 410 km discontinuity sharpness and the form of the olivine alpha-beta phase diagram: Resolution of apparent seismic contradictions. Geophys J Int'l 126:F7-F12
Hemley RJ, Cohen RE (1996) Structure and bonding in the deep mantle and core. Phil Trans R Soc Lond A354:1461-1479
Herzberg CT, O'Hara MJ (1985) Origin of mantle peridotite and komatiite by partial melting. Geophys Res Lett 12:541-544
Hoffmann AW (1997) Mantle geochemistry: The message from oceanic volcanism. Nature 385:219-229
Holweger H, Heise C, Kock M (1990) The abundance of iron in the Sun derived from photospheric Fe II lines. Astron Astrophys. 232:510-515
Honkura Y, Abe T, Matsushima M (1996) Global electrical conductivity distribution in the mantle based on the P_1^0 approximation. Eos Trans Am Geophys Union 77:F167
Irifune T, Isshiki M (1998) Iron partitioning in a pyrolite mantle and the nature of the 410km seismic discontinuity. Nature 392:702-705
Irifune T, Koizumi T, Ando J (1996) An experimental study of the garnet-perovskite transformation in the system $MgSiO_3$-$Mg_3Al_2Si_3O_{12}$. Phys Earth Planet Inter 96:147-157
Isaak DG, Cohen RE, Mehl MJ (1990) Calculated elastic and thermal properties of MgO at high pressure and temperatures. J Geophys Res 95:7055-7067
Ito E, Katsura T (1989) A temperature profile of the mantle transition zone. Geophys Res Lett 16:425-428
Jackson I (1983) Some geophysical constraints on the chemical composition of the Earth's lower mantle. Earth Planet Sci Lett 62:91-103
Jackson I (1998a) Elasticity, composition and temperature of the Earth's lower mantle: A reappraisal. Geophys J Int'l 134:291-311
Jackson I (1998b) Laboratory measurements of seismic wave dispersion and attenuation: Recent progress. *In:* S Karato (ed) Mineral Physics and Seismic Tomography (submitted) American Geophysical Union, Washington, DC
Jackson I, Rigden SM (1998) Composition and temperature of the Earth's mantle: Seismological models interpreted through experimental studies of Earth materials. *In:* I Jackson (ed) The Earth's Mantle: Composition, Structure and Evolution p 405-460 Cambridge University, Cambridge
Jeanloz R (1995) Earth dons a different mantle. Nature 378:130-131
Jeanloz R, Knittle E (1989) Density and composition of the lower mantle. Phil Trans R Soc Lond A328:377-389
Jeffreys, H (1936) Geophysical discussion. Observatory 59:267-268
Johnson CL, Constable CG (1997) The time-averaged geomagnetic field: Global and regional biases for 0-5 Ma. Geophys J Int'l 131:643-666
Johnson CL, Constable CG (1998) Persistently anomalous Pacific geomagnetic fields. Geophys Res Lett 25:1011-1014
Kaneshima S, Helffrich G (1998) Detection of lower mantle scatterers northeast of the Mariana subduction zone using short-period array data. J Geophys Res 103: 4825-4838
Kaneshima S, Silver PG (1995) Anisotropic loci in the mantle beneath central Peru. Phys Earth Planet Inter 88:257-272
Karato S (1990) The role of hydrogen in the electrical conductivity of the upper mantle. Nature 347:272-273
Karato S (1993) Importance of anelasticity in the interpretation of seismic tomography. Geophys Res Lett 20:1623-1626
Karato S (1997) Phase transformations and rheological properties of mantle minerals. *In:* DJ Crossley (ed) Earth's Deep Interior, The Doornbos Memorial Volume p 223-272 Gordon and Breach, Amsterdam
Karato S (1998a) Seismic anisotropy in the deep mantle, boundary layers and the geometry of mantle convection. Pure Appl Geophys 151:565-587
Karato S (1998b) A dislocation model of seismic wave attenuation and micro-creep in the Earth: Harold Jeffreys and the rheology of the solid Earth. Pure Appl Geophys (in press)
Karato S-I (1998c) Micro-physics of post glacial rebound. GeoResearch Forum 3/4:351-364
Karato S (1998d) Some remarks on the origin of seismic anisotropy in the D" layer. Earth Planets Space (in press)
Karato S, Jung H (1998) Water, partial melting and the origin of the seismic low velocity and high attenuation zone in the upper mantle. Earth Planet Sci Lett 157:193-207
Karato S, Li P (1992) Diffusion creep in perovskite: Implications for the rheology of the lower mantle. Science 255:1238-1240
Karato S, Wu P (1993) Rheology of the upper mantle: A synthesis. Science 260:771-778
Karki BB, Stixrude L, Clark SJ, Warren MC, Ackland GJ, Crain J (1997a) Structure and elasticity of MgO at high pressure. Am Mineral 82:51-60
Karki BB, Stixrude L, Clark SJ, Warren MC, Ackland GJ, Crain J (1997b) Elastic properties of $MgSiO_3$ perovskite at lower mantle pressures. Am Mineral 82:635-638
Kato T, Ringwood AE, Irifune T (1988) Experimental determination of element partitioning between silicate perovskites, garnets and liquids: Constraints on early differentiation of the mantle. Earth Planet Sci Lett 89:123-145
Kawakatsu H, Niu F (1994) Seismic evidence for a 920-km discontinuity in the mantle. Nature 371:301-305
Kellogg LH (1992) Mixing in the mantle. Ann Rev Earth Planet Sci 20:365-388
Kellogg LH (1993) Chaotic mixing in the earth's mantle. Advan Geophys 34:1-33
Kendall JM, Silver PG (1996) Constraints from seismic anisotropy on the nature of the lowermost mantle. Nature 381:409-412
Kennett BLN (1975) The effects of attenuation on seismograms. Bull Seis Soc Am 65:1643-1651
Kennett BLN, Engdahl ER (1991) Traveltimes for global earthquake location and phase identifications. Geophys J Int'l 105:429-465
Kennett BLN, Engdahl ER, Buland R (1995) Constraints on seismic velocities in the Earth from travel times. Geophys J Int'l 122:108-124
Kesson SE, Fitz Gerald JD (1991) Partitioning of MgO, FeO, NiO, MnO and Cr_2O_3 between magnesian silicate perovskite and magnesiowüstite: Implications for the origin of inclusions in diamond and the composition of the lower mantle. Earth Planet Sci Lett 111:229-240
Kesson SE, Fitzgerald JD, Shelley JMG (1998) Mineralogy and dynamics of a pyrolite lower mantle. Nature 393:252-255
Kido M, Čadek O (1997) Inferences of viscosity from the oceanic geoid: Indication of a low viscosity zone below the 660-km discontinuity. Earth Planet Sci Lett 151:125-137
King SD (1995) Models of mantle viscosity. *In:* TJ Ahrens (ed) Mineral Physics and Crystallography: A Handbook of Physical Constants p 227-236 American Geophysical Union, Washington, DC

King SD, Masters G (1992) An inversion for radial viscosity structure using seismic tomography. Geophys Res Lett 19:1551-1554
Kingma KJ, Cohen RE, Hemley RJ, Mao HK (1995) Transformation of stishovite to a denser phase at lower mantle pressures. Nature 374:243-245
Knittle et al. (1986) Knittle E, Jeanloz R, Smith GL (1986) Thermal expansion of silicate perovskite and stratification of the Earth's mantle. Nature 319:214-216
Lahiri B, Price A (1939) Electromagnetic induction in non-uniform conductors, and the determination of the conductivity of the Earth from terrestrial magnetic variations. Phil Trans R Soc Lond 237:509-540
Lay T, Wallace TC (1995) Modern Global Seismology. Academic, San Diego, California
le Stunff Y, Wicks CW Jr, Romanowicz B (1995) P'P' precursors under Africa: Evidence for mid-mantle reflectors. Science 270:74-77
Li X, Jeanloz R (1991a) Effect of iron content on the electrical conductivity of perovskite and magnesiowüstite assemblages at lower mantle conditions. J Geophys Res 96:6113-6120
Li X, Jeanloz R (1991b) Phases and electrical conductivity of a hydrous silicate assemblage at lower-mantle conditions. Nature 350:332-334
Li X, Ming L-C, Manghnani MH, Wang Y, Jeanloz R (1993) Pressure dependence of the electrical conductivity of $(Mg_{0.9}Fe_{0.1})SiO_3$ perovskite. J Geophys Res 98:501-508
Li XD, Romanowicz B (1996) Global mantle shear velocity model developed using nonlinear asymptotic coupling theory. J Geophys Res 101:22245-22272
Lithgow-Bertelloni C, Richards MA (1998) The dynamics of Cenozoic and Mesozoic plate motions. Rev Geophys 36:27-78
Liu X-F, Tromp J, Dziewonski AM (1998) Is there a first-order discontinuity in the lowermost mantle? Earth Planet Sci Lett (in press)
Mao HK (1988) The 670-km discontinuity in the mantle: A bulk chemical composition boundary driven by phase transformation. Eos Trans Am Geophys Union 69:1420
Mao HK, Shen G, Hemley RJ (1997) Multivariable dependence of Fe/Mg partitioning in the Earth's lower mantle. Science 278:2098-2100
Mao, HK, Shu J, Fei Y, Hu J, Hemley RJ (1996) The wüstite enigma. Phys Earth Planet Inter 96:135-145
Marton FC, Cohen RE (1994) Prediction of a high-pressure phase transition in Al_2O_3. Am Mineral 79:789-792
Masters G (1979) Observational constraints on the chemical and thermal structure of the Earth's deep interior. Geophys J R Astr Soc 57:507-534
Matzel E, Sen MK, Grand SP (1996) Evidence for anisotropy in the deep mantle beneath Alaska. Geophys Res Lett 23:2417-2420
McCammon CA (1997) Perovskite as a possible sink for ferric iron in the lower mantle. Nature 387: 694-696
McDonough WF, Sun S (1995) The composition of the Earth. Chem Geol 120:223-253
McMillan PF, Hemley RJ, Gillet P (1996) Vibrational spectroscopy of mantle minerals. *In:* MD Dyar, C McCammon, MW Schaefer (eds) Mineral Spectroscopy: A Tribute to Roger G. Burns p 175-213 Geochemical Society
Meade C, Reffner JA, Ito E (1994) Synchrotron infrared absorbance measurements of hydrogen in $MgSiO_3$ perovskite. Science 264:1558-1560
Meade C, Silver PG, Kaneshima S (1995) Laboratory and seismological observations of lower mantle isotropy. Geophys Res Lett 22:1293-1296
Melbourne T, Helmberger D (1998) Fine structure of the 410-km discontinuity. J Geophys Res 103:10091-10102
Metcalfe G, Bina CR, Ottino JM (1995) Kinematic considerations for mantle mixing. Geophys Res Lett 22:743-746
Mitrovica JX (1996) Haskell (1935) revisited. J Geophys Res 101:555-569
Montagner J-P, Kennett BLN (1996) How to reconcile body-wave and normal-mode reference earth models. Geophys J Int'l 125:229-248
Montagner J-P, Tanimoto T (1991) Global upper mantle tomography of seismic velocities and anisotropies. J Geophys Res 96:20337-20351
Morelli A, Dziewonski AM (1993) Body wave traveltimes and a spherically symmetric P- and S-wave velocity model. Geophys J Int'l 112:178-194
Navrotsky A (1994) Physics and Chemistry of Earth Materials. Cambridge University, Cambridge
Niu F, Kawakatsu H (1997) Depth variation of the mid-mantle seismic discontinuity. Geophys Res Lett 24:429-432
Nolet G (1990) Partitioned waveform inversion and two-dimensional structure under the network of autonomously recording seismographs. J Geophys Res 95:8499-8512
Nolet G, Moser TJ (1993) Teleseismic delay times in a 3-D Earth and a new look at the S-discrepancy. Geophys J Int'l 114:185-195
Okal EA, Jo B-G (1990) Q measurements for phase X overtones. Pure Appl Geophys 132:331-362
Pawley, AR, McMillan PF, Holloway JR (1993) Hydrogen in stishovite, with implications for mantle water

content. Science 261:1024-1026
Petersons HF, Constable SC (1996) Global mapping of the electrically conductive lower mantle. Geophys Res Lett 23:1461-1464
Peyronneau J, Poirier J-P (1989) Electrical conductivity of the Earth's lower mantle. Nature 342:537-539
Poirier J-P, Tarantola A (1998) A logarithmic equation of state. Phys Earth Planet Inter (in press)
Poirier J-P (1981) Martensitic olivine-spinel transformation and plasticity of the mantle transition zone. *In:* FD Stacey, MS Paterson, A Nicolas (eds) Anelasticity in the Earth p 113-117 American Geophysical Union, Washington, DC
Ravine MA, Phipps Morgan J (1993) Geoid effects of lateral viscosity variation near the top of the mantle: A 2-D model. Earth Planet Sci Lett 119:617-625
Revenaugh J, Jordan TH (1991a) Mantle layering from ScS reverberations: 1. Waveform inversion of zeroth-order reverberations. J Geophys Res 96:19749-19762
Revenaugh J, Jordan TH (1991b) Mantle layering from ScS reverberations: 4. The lower mantle and core-mantle boundary. J Geophys Res 96:19811-19824
Reynard B, Fiquet G, Itié J-P, Rubie DC (1996) High-pressure X-ray diffraction study and equation of state of $MgSiO_3$-ilmenite. Am Mineral 81:45-50
Reynard B, Rubie DC (1996) High-pressure high-temperature Raman spectroscopic study of ilmenite-type $MgSiO_3$. Am Mineral 81:1092-1096
Ribe, NM (1989) Seismic anisotropy and mantle flow. J Geophys Res 94:4213-4223
Ringwood, AE (1975) Composition and Petrology of the Earth's Mantle. McGraw-Hill, New York
Ringwood, AE (1989) Constitution and evolution of the mantle. Spec Pub Geol Soc Australia 14:457-485
Roberts RG (1986) The deep electrical structure of the Earth. Geophys J R Astr Soc 85:583-600
Robertson GS, Woodhouse JH (1996) Constraints on lower mantle physical properties from seismology and mineral physics. Earth Planet Sci Lett 143:197-205
Romanowicz B (1987) Multiplet-multiplet coupling due to lateral heterogeneity: Asymptotic effects on the amplitude and frequency of the Earth's normal modes. Geophys J R Astron Soc 90:75-100
Romanowicz B (1994) Anelastic tomography: A new perspective on the upper mantle thermal structure. Earth Planet Sci Lett 128:113-121
Romanowicz B (1997) 3D models of elastic and anelastic structure in the mantle. Eos Trans Am Geophys Union 78:F466
Romanowicz B (1998) Attenuation tomography of the Earth's mantle: A review of current status. Pure Appl Geophys (in press)
Rubie DC, Brearley AJ (1994) Phase transformations between β and γ $(Mg, Fe)_2SiO_4$ in the Earth's mantle: Mechanisms and rheological implications. Science 264:1445-1448
Russo RM, Silver PG, Franke M, Ambeh WB, James DE (1996) Shear-wave splitting in northeast Venezuela, Trinidad, and the eastern Caribbean. Phys Earth Planet Inter 95:251-275
Sambridge M, Gudmundsson O (1998) Tomography with irregular cells. J Geophys Res 103:773-781
Schultz A (1990) On the vertical gradient and lateral heterogeneity in mid-mantle electrical conductivity. Phys Earth Planet Inter 64:68-86
Schultz A, Larsen JC (1987) On the electrical conductivity of the mid-mantle: 1—Calculation of equivalent scalar magnetotelluric response functions. Geophys J R Astr Soc 88:733-761
Schultz A, Larsen JC (1990) On the electrical conductivity of the mid-mantle: 2—Delineation of heterogeneity by application of extremal inverse solutions. Geophys J R Astr Soc 101:565-580
Schultz A, Pritchard G (1995) Inversion for the three-dimensional structure of the Earth's mantle: Rapid convergence through spectral methods, stiff solvers and interpolation and integration on a convex hull. *In:* Three-Dimensional Electromagnetics, Proceedings of an International Symposium in Honor of Jerry Hohmann p 429-452 Schlumberger-Doll Research, Ridgefield, Connecticut
Schultz A, Pritchard G (1998) A three-dimensional inversion for large-scale structure in a spherical domain. *In:* M Oristaglio, B Spiess (eds) Three-Dimensional Electromagnetics (in press) Society of Exploration Geophysics, Tulsa, Oklahoma
Shankland TJ, Peyronneau J, Poirier J-P (1993) Electrical conductivity of the Earth's lower mantle. Nature 366:453-455
Shearer PM (1991a) Constraints on upper mantle discontinuities from observations of long-period reflected and converted phases. J Geophys Res 96:18147-18182
Shearer PM (1991b) Imaging global body wave phases by stacking long-period seismograms. J Geophys Res 96:20353-20364
Silver PG (1996) Seismic anisotropy beneath the continents: Probing the depths of geology. Ann Rev Earth Planet Sci 24:385-432
Silver PG, Bina CR (1993) An anomaly in the amplitude ratio of SKKS/SKS in the range 100-108° from portable teleseismic data. Geophys Res Lett 20:1135-1138
Silver PG, Chan WW (1988) Implications for continental structure and evolution from seismic anisotropy. Nature 335:34-39
Silver PG, Chan WW (1991) Shear-wave splitting and subcontinental mantle deformation. J Geophys Res 96:16429-16454

Silver PG, Savage M (1994) The interpretation of shear-wave splitting parameters in the presence of two anisotropic layers. Geophys J Int'l 119:949-963
Sipkin S, Jordan TH (1979) Frequency dependence of Q_{ScS}. Bull Seism Soc Am 69:1055-1079
Spakman W, Nolet G (1988) Imaging algorithms, accuracy and resolution in time delay tomography. *In:* NJ Vlaar, G Nolet, MJR Wortel, SAPL Cloetingh (eds) Mathematical Geophysics p 155-187 Reidel, Dordrecht
Spakman W, Stein S, van der Hilst R, Wortel R (1989) Resolution experiments for NW Pacific subduction zone tomography. Geophys Res Lett 16:1097-1100
Stacey FD (1998) Thermoelasticity of a mineral composite and a reconsideration of lower mantle properties. Phys Earth Planet Inter 106:219-236
Stewart DN, Busse F H, Whaler KA, Gubbins D (1995) Geomagnetism, Earth rotation and the electrical conductivity of the lower mantle. Phys Earth Planet Inter 92:199-214
Su W, Woodward RL, Dziewonski AM (1994) Degree 12 model of shear velocity heterogeneity in the mantle. J Geophys Res 99:6945-6980
Tajima F, Fukao Y, Obayashi M, Sakurai T (1998) Evaluation of slab images in the northwestern Pacific. Earth Planet Space (in press)
Tsuchida Y, Yagi T (1989) A new, post-stishovite high-pressure polymorph of silica. Nature 340:217-220
Vacher P, Mocquet A, Sotin C (1998) Computation of seismic profiles from mineral physics: The importance of the non-olivine components for explaining the 660 km depth discontinuity. Phys Earth Planet Inter 106:275-298
VanDecar JC, James DE, Assumpçaõ M (1995) Seismic evidence for a fossil mantle plume beneath South America and implications for plate driving forces. Nature 378:25-31
van der Hilst RD, Engdahl ER, Spakman W (1989) Importance of the reference model in linearized tomography and image of subduction below the Caribbean plate. Geophys Res Lett 16:1093-1096
van der Hilst RD, Engdahl ER, Spakman W (1993) Tomographic inversion of P and pP data for aspheric mantle structure below the northwest Pacific region. Geophys J Int'l 115:264-302
van der Hilst RD, Widiyantoro S, Engdahl ER (1997) Evidence for deep mantle circulation from global tomography. Nature 386:578-589
van der Lee S, Nolet G (1997) Seismic image of the subducted trailing fragments of the Farallon plate. Nature 386:266-269
van der Lee S, Paulssen H, Nolet G (1994) Variability of P660s phases as a consequence of topography of the 660 km discontinuity. Phys Earth Planet Inter 86:147-164
Vinnik LP, Kosarev GL, Makeyeva LI (1984) Anizotropiya litosfery po nablyudeniyam voln SKS and SKKS. Dokl Akad Nauk USSR 278:1335-1339
Vinnik L, Montagner J-P (1996) Shear wave splitting in the mantle Ps phases. Geophys Res Lett 23:2449-2452
Vinnik LP, Romanowicz B, le Stunff Y, Makeyeva L (1995) Seismic anisotropy in the D" layer. Geophys Res Lett 22:1657-1660
Walck MC (1984) The P-wave upper mantle structure beneath an active spreading center: The Gulf of California. Geophys J R Astron Soc 76:697-723
Wang Y, Martinez I, Guyot F, Liebermann RC (1997) The breakdown of olivine to perovskite and magnesiowüstite. Science 275:510-513
Wang Y, Weidner DJ, Guyot F (1996) Thermal equation of state of $CaSiO_3$ perovskite. J Geophys Res 101: 661-672
Weinstein SA (1992) Induced compositional layering in a convecting fluid layer by an endothermic phase transition. Earth Planet Sci Lett 113:23-39
Widmer R, Masters G, Gilbert F (1993) Spherically symmetric attenuation within the Earth from normal mode data. Geophys J Int'l 104:541-553
Williams Q, Garnero EJ (1996) Seismic evidence for partial melt at the base of Earth's mantle. Science 273:1528-1530
Wolfe CJ, Bjarnason ITh, VanDecar JC, Solomon SC (1997) Seismic structure of the Iceland mantle plume. Nature 385:245-247
Wood BJ (1995) The effect of H_2O on the 410 km seismic discontinuity. Science 268:74-78
Wood BJ, Pawley A, Frost DR (1996) Water and carbon in the Earth's mantle. Phil Trans R Soc Lond A354:1495-1511
Wood BJ, Rubie DC (1996) The effect of alumina on phase transformations at the 660-kilometer discontinuity from Fe-Mg partitioning experiments. Science 273:1522-1524
Woodland AB, Angel RJ (1998) Crystal structure of a new spinelloid with the wadsleyite structure in the system Fe_2SiO_4-Fe_3O_4 and implications for the Earth's mantle. Am Mineral 83:404-408
Wysession ME, Okal EA, Bina CR (1992) The structure of the core-mantle boundary from diffracted waves. J Geophys Res 97:8749-8764
Zhao D, Hasegawa A (1993.) P wave tomographic imaging of the crust and upper mantle beneath the Japan Islands. J Geophys Res 98:4333-4353
Zhao D, Hasegawa A, Kanamori H (1994) Deep structure of Japan subduction zone as derived from local, regional and teleseismic events. J Geophys Res 99:22313-22329
Zhao Y, Anderson DL (1994) Mineral physics constraints on the chemical composition of the Earth's lower mantle. Phys Earth Planet Inter 85:273-292
Zhou H-W, Clayton RW (1990) P and S wave travel time inversion for subducting slab under the island arcs of the northwest Pacific. J Geophys Res 95:6829-6851
Zhang S, Christensen UR (1993) Some effects of lateral viscosity variations on geoid and surface velocities induced by density anomalies in the mantle. Geophys J Int'l 114:531-547
Zhang S, Yuen DA (1995) The influence of lower mantle viscosity stratification on 3D spherical-shell mantle convection. Earth Planet Sci Lett 132:157-166
Zielhuis A, Nolet G (1994) Shear-wave velocity variations in the upper mantle beneath central Europe. Geophys J Int'l 117:695-715
Zindler A, Hart S (1986) Chemical geodynamics. Ann Rev Earth Planet Sci 14:493-571

Reviews in Mineralogy, Volume 37
Ultrahigh-Pressure Mineralogy

Chapter 6

LOWER MANTLE MINERALOGY AND THE GEOPHYSICAL PERSPECTIVE

Craig R. Bina

Department of Geological Sciences
Northwestern University
Evanston, Illinois 60208

ERRATA

Page 207:

Note that panels **b** and **c** in Figure 1 have been transposed.

Page 219:

The subsection heading ***V_P / V_S relations*** should be set in bold italics rather than italics.

Page 232:

In the last paragraph of the chapter, the following sentence was garbled:

> "With regard to the oxides, FeO undergoes transformation to a rhombohedral structure at pressures corresponding to ~1700 km (Mao et al. 1996), perhaps shifting to shallower depths in (Mg,Fe)O magnesiowüstite."

The correct sentence should read as follows:

> With regard to the oxides, while FeO wüstite undergoes transformation to a rhombohedral structure at upper mantle pressures (and perhaps at slightly higher pressures in some (Mg,Fe)O magnesiowüstites), it transforms to a NiAs-type structure at pressures corresponding to ~1700 km (Mao et al. 1996).

Page 231:

Similarly, the dotted line in Figure 12 labelled $\frac{wust}{rhomb}$ should actually be labelled $\frac{rhomb}{NiAs}$.

Below are two additional panels, to supplement those in Figure 11 [page 230] and Figure 12 [page 231], which may be of some interest.

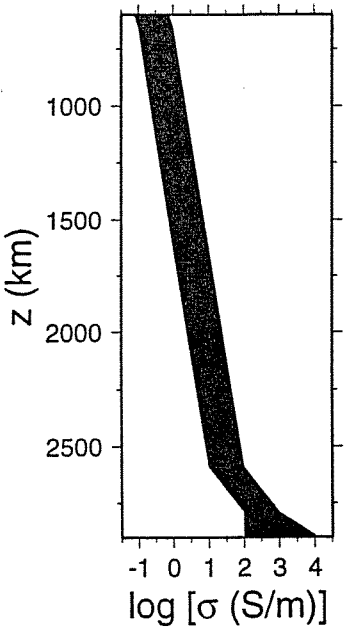

(electrical conductivity)

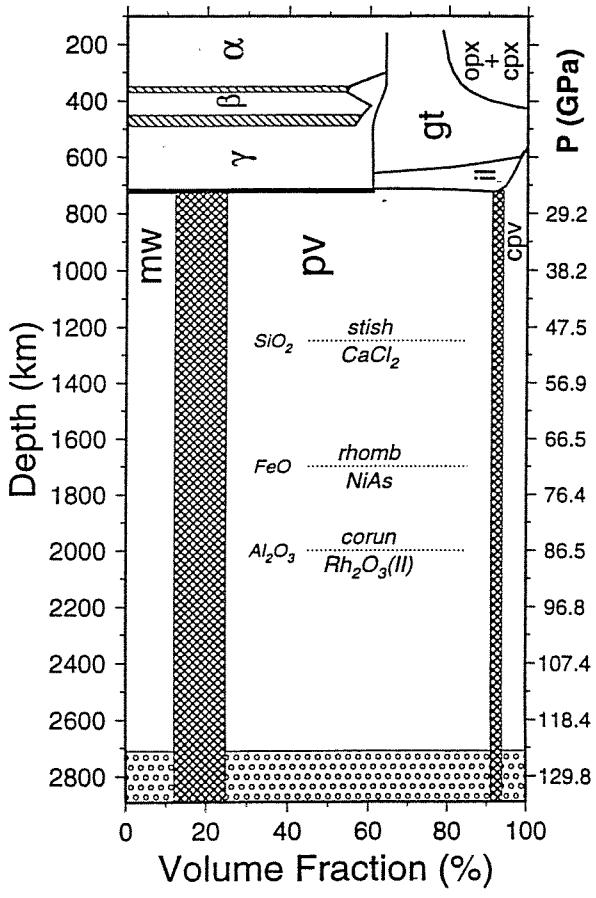

(subduction zones)